PYTHON package for dark matter scattering in dielectric targets

Simon Knapen[®], ^{1,*} Jonathan Kozaczuk, ^{2,†} and Tongyan Lin^{2,‡} ¹CERN, Theoretical Physics Department, Espl. des Particules 1, 1211 Meyrin, Switzerland ²Department of Physics, University of California, San Diego, California 92093, USA

(Received 15 November 2021; accepted 20 December 2021; published 12 January 2022)

We present *DarkELF*, a PYTHON package to calculate interaction rates of light dark matter in dielectric materials, including screening effects. The full response of the material is parametrized in the terms of the energy loss function (ELF) of material, which *DarkELF* converts into differential scattering rates for both direct dark matter electron scattering and through the Migdal effect. In addition, *DarkELF* can calculate the rate to produce phonons from sub-MeV dark matter scattering via the dark photon mediator, as well as the absorption rate for dark matter comprised of dark photons. The package includes precomputed ELFs for Al, Al₂O₃, GaAs, GaN, Ge, Si, SiO₂, and ZnS, and allows the user to easily add their own ELF extractions for arbitrary materials.

DOI: 10.1103/PhysRevD.105.015014

I. INTRODUCTION

The search for the direct detection of the dark matter has progressed to a phase where there are numerous experiments aiming to probe sub-GeV dark matter (DM), often by leveraging electronic excitations, see, e.g., [1–4]. In addition the next generation of detectors is aiming for energy thresholds well below the ionization threshold of the target [5,6], thus opening the path to search for individual phonon excitations. For all such strategies, the many-body physics of the target material is important and detailed calculations at the interface with condensed matter physics are therefore needed to accurately extract the relevant scattering rates.

Electron excitations may arise from direct DM-electron scattering [7–11], as shake-off electrons from nuclear recoils [12–14] or from secondary ionizations as the recoiling nucleus travels through the target material. Solid state targets are particularly advantageous because they can have arbitrarily small gaps to produce electron excitations. However, because their electron wave functions are delocalized and highly nontrivial, calculations of the differential scattering rate are often involved and material dependent. For Si and Ge targets, Essig *et al.* [10] performed the first calculation of DM-electron scattering using electronic wave functions obtained with density

Published by the American Physical Society under the terms of the Creative Commons Attribution 4.0 International license. Further distribution of this work must maintain attribution to the author(s) and the published article's title, journal citation, and DOI. Funded by SCOAP³. functional theory (DFT). This calculation was subsequently applied to a broader range of semiconductors [15,16].

It was recently pointed out that the DM-electron scattering rate can be extracted directly from the energy loss function (ELF)

$$\operatorname{Im}\left[\frac{-1}{\varepsilon(\boldsymbol{\omega}, \mathbf{k})}\right] \tag{1}$$

of the target material [17,18], where $\epsilon(\omega, \mathbf{k})$ is the momentum and frequency dependent longitudinal dielectric function. This approach has two main advantages: (i) In-medium screening effects are automatically included and were found to reduce the scattering rate by a nonnegligible amount (ii) The ELF is exceptionally wellstudied experimentally and theoretically in the materials science literature, which means that standard and well validated tools can be used to extract it for the target of interest. In [17], we calculated the ELF for Si and Ge using time-dependent density functional theory (TDDFT) methods with the GPAW package [19,20] and compared this method with an approach fitting data to a Mermin oscillator model [21,22]. We elaborate on these methods and their advantages and shortcomings in Sec. II. We found both methods to be in excellent agreement in the regime most relevant for DM-electron scattering, as discussed in Sec. III.

Even if the DM couples predominantly to nuclei, it can still leave an electronic signal in the detector. One way this could happen is if the nucleus "shakes-off" an electron during the initial hard recoil [12–14]. This is known as the Migdal effect [23,24], and has been applied extensively to DM scattering off atomic targets [25–34]. References [35,36] provided the first full derivation of the Migdal effect for dark matter scattering in semiconductors, showing that it can be

simon.knapen@cern.ch jkozaczuk@physics.ucsd.edu

^{*}tongyan@physics.ucsd.edu

treated as an in-medium analog of bremsstrahlung. The ELF again plays a critical role, as it determines the probability for the nucleus to shake-off an electron. In Sec. IV we summarize our results of [35], present a few new computations, and discuss their implementation in *DarkELF*.

Neither the Migdal effect nor direct electron recoils are available if the kinetic energy of the DM is below the electron bandgap of the target. In this case the dark matter can still deposit energy by producing one or more athermal phonons in the target. Such processes have been studied extensively in both superfluid He [37-42] and solid state targets [15,16,43–49]. Given the existing constraints on models of sub-MeV dark matter, DM scattering through a dark photon mediator and dark photon DM absorption appear to be the most promising processes [50]. Both are most pronounced in polar materials [43,44] and can be modeled with the ELF, for frequencies below the band gap of the target. Previous calculations rather heavily relied on computationally intensive DFT methods, though analytical approximations are available some instances. Here we present an intermediate method, where we write the rate in terms of the ELF, which we subsequently take from experimental data. For phonon-scattering and absorption processes we moreover only need to know the ELF in the low momentum (optical) limit, for which good experimental measurements are readily available. The ELF method is more accurate than the existing analytical approximations, while bypassing the time-consuming DFT calculations. DM-phonon scattering and dark photon absorption are discussed in Secs. V and VI, respectively.

DarkELF is available at https://github.com/tongylin/ DarkELF and comes with tabulated ELFs for Al₂O₃, GaN, Al, ZnS, GaAs, SiO₂, Si, and Ge, allowing the user to easily calculate differential DM scattering rates in these materials. Additional materials and ELF extractions may be added to the repository as the need arises. Users can compute the rate subject to various fiducial cuts, or implement their own form factors to study nonstandard DM models. It is also straightforward for a user to add their own calculations or extractions of the ELF, facilitating fast comparisons between methods and materials. This makes DarkELF also a suitable tool for target optimization and to study the theoretical uncertainties associated with the scattering rate. In Sec. VII we offer some concluding remarks and comment on possible future additions to the code. For instruction on the usage of *DarkELF*, we refer to the Appendix and the example jupyter [51] notebooks in the repository. The example notebooks also contain a number of additional plots which were omitted in the paper for brevity.

II. CALCULATING THE ELF

The ELF describes the energy loss of a charged particle traveling through the material. It is therefore not only of practical importance, but also provides a window into the physical mechanisms at play in the target. Furthermore detailed first-principles calculations of the ELF are now possible, which can be compared with experimental data. For our purposes, this means that there a number of complementary methods which one can use to compute the ELF, and comparing them can give us some insight in the uncertainties associated with dark matter interactions with the target material.

DarkELF is set up independently of the method used to calculate the ELF, as the real and imaginary components of the dielectric function (ϵ_1, ϵ_2) are read in as a look-up table. The user can therefore supply their own calculation of the ELF and straightforwardly extract the dark matter interaction rates. We also supply a number of precomputed look-up tables with the code. Note that everywhere in this work, dielectric function refers exclusively to the longitudinal dielectric function. We will also work in the approximation that both the ELF and dielectric function are isotropic in momentum and diagonal in reciprocal lattice space [17].

In this section, we focus on the ELF for $\omega > E_{\rm gap}$, with $E_{\rm gap}$ the electron band gap, where the energy loss is dominated by the electron response of the material. Below the electron band gap, the leading contribution to the ELF will generally be phonons, which will be discussed in Sec. V. For the electron-response regime, we supply results for three independent methods to compute the ELF:

(i) The Lindhard method is the most simplistic and uses the Lindhard dielectric function, which models the material as a noninteracting Fermi liquid. The main advantage of using the Lindhard dielectric function is its simplicity, as it depends only on the plasma frequency (ω_p) , or equivalently, the Fermi velocity [52]:

$$\epsilon_{\text{Lin}}(\omega, k) = 1 + \frac{3\omega_p^2}{k^2 v_E^2 \eta^{-0}} \left[f\left(\frac{\omega + i\eta}{k v_E}, \frac{k}{2m_e v_E}\right) \right]$$
(2)

with

$$v_F = \left(\frac{3\pi\omega_p^2}{4\alpha m_e^2}\right)^{1/3}$$

$$f(u, z) = \frac{1}{2} + \frac{1}{8z}[g(z - u) + g(z + u)]$$

$$g(x) = (1 - x^2)\log\left(\frac{1 + x}{1 - x}\right)$$

with α and m_e respectively the fine structure constant and the electron mass. The Lindhard dielectric function approximates the material as homogeneous and neglects all dissipation effects. This means that the plasmon pole is infinitely narrow, an approximation which is badly violated in most semiconductors. For halo DM, however, scattering is

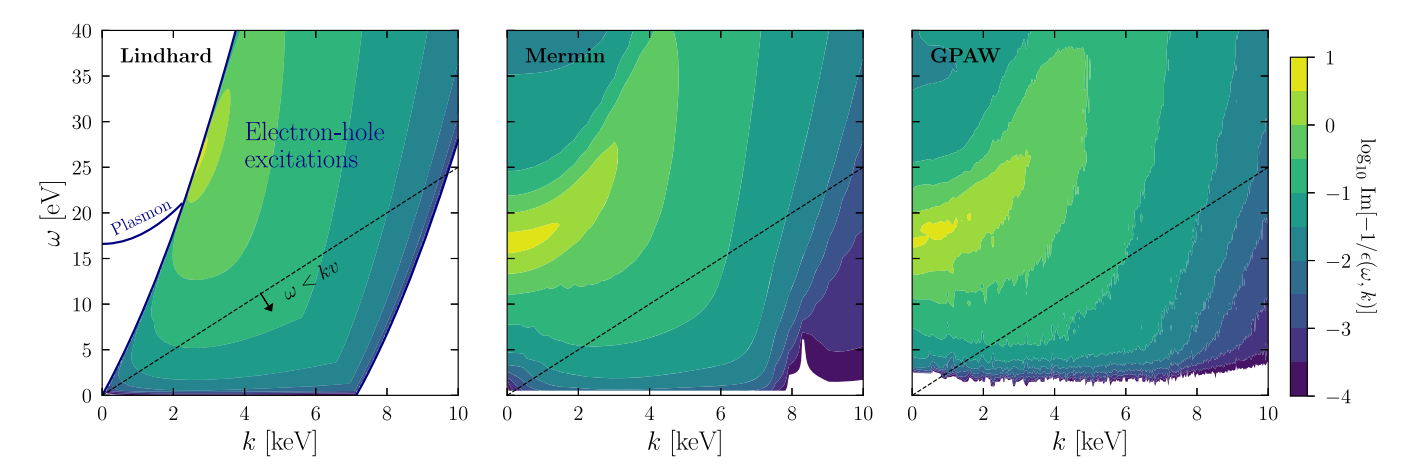


FIG. 1. ELF for Si, calculated using the Lindhard, Mermin, and GPAW methods, as described in the text. The blue line in the left-hand panel indicates the location of plasmon pole, which is a Dirac delta-function in the Lindhard method. Only the GPAW method (right-hand panel) correctly models the low ω regime, close to the band gap. For halo DM scattering off electrons, the accessible phase space is bounded by $\omega < kv$, which is indicated by the dashed line with $v = 2.5 \times 10^{-3}$.

dominated by the production of electron-hole pairs far away from the plasmon pole, which can be modeled qualitatively with the Lindhard ELF. This is shown in the left-hand panel of Fig. 1. The Lindhard ELF does not provide an accurate description of realistic semiconductors at low k and high ω , and therefore cannot be used for absorption processes.

(ii) The Mermin method is a generalization of the Lindhard method which includes dissipation and can also be used for absorption processes. Concretely, a dissipation parameter Γ can be added to the Lindhard model in a self-consistent way by defining the Mermin dielectric function [21]

$$\epsilon_{\mathrm{Mer}}(\omega,k) = 1 + \frac{(1+i\frac{\Gamma}{\omega})(\epsilon_{\mathrm{Lin}}(\omega+i\Gamma,k)-1)}{1+(i\frac{\Gamma}{\omega})\frac{\epsilon_{\mathrm{Lin}}(\omega+i\Gamma,k)-1}{\epsilon_{\mathrm{Ci}}(0,k)-1}}.$$
 (3)

In the Mermin method, the ELF is modeled as a superposition of ELFs obtained with the Mermin dielectric function, where the plasma frequencies, dissipation parameters and the weights of the different terms are fitted to experimental data. In an ad hoc way, this weighted linear combination accounts for the inhomogeneities in the electron number density within the unit cell. The fitted data typically includes the measured ELF from reflection electron energy loss spectroscopy (REELS) and/or optical data (k = 0 limit), and therefore can reproduce absorption processes. The theoretically motivated ansatz in (3) provides a way to perform a controlled extrapolation of the ELF to finite k, while conserving local electron number. Experimental collaborations [53–55] moreover occasionally present their results in terms of fits to models whose parameters can be reinterpreted in terms of the Mermin model. This reinterpretation is done with the +CHAPIDIF+ package [22], which builds on the work in [56–58]. For more details about our procedure we refer to our earlier work in [17].

The middle panel of Fig. 1 shows the ELF for Si, as obtained with the Mermin method applied to the experimental data in [54]. The low k region near the plasmon pole is much more realistic than for the Lindhard ELF, as this is the regime where the ansatz is fit to the experimental data. Even with a finite width, the plasmon region is still well outside the kinematically allowed regime for DM-electron scattering, as indicated by the dashed black line. The Mermin method however does not incorporate the detailed band structure of the material. In particular, in the middle panel of Fig. 1 one can see that it effectively predicts a vanishing band gap, which is of course not realistic for a semiconductor such as Si. As we will see, it is also less appropriate to model the high momentum ($k \gtrsim 15 \text{ keV}$) regime.

(iii) The GPAW method is the most sophisticated of the three methods we employ, as it relies on a first-principles TDDFT calculation with the software package GPAW [19,20]. In this method one approximates the many-body electron wave functions with a Kohn-Sham (KS) system [62] of effective, single particle wave functions subject to an effective potential. This system is then solved numerically on a periodic lattice. The GPAW method does the best job in modeling the detailed properties of the material, in particular for ω near the band gap.

¹The band gap can be approximated by the *ad hoc* addition of a Heaviside step function $\theta(\omega-E_{\rm gap})$ [59] or with the Mermin-Levine-Louie ansatz (MLL) [60]. See Refs. [56,61] for comparisons between these various approaches.

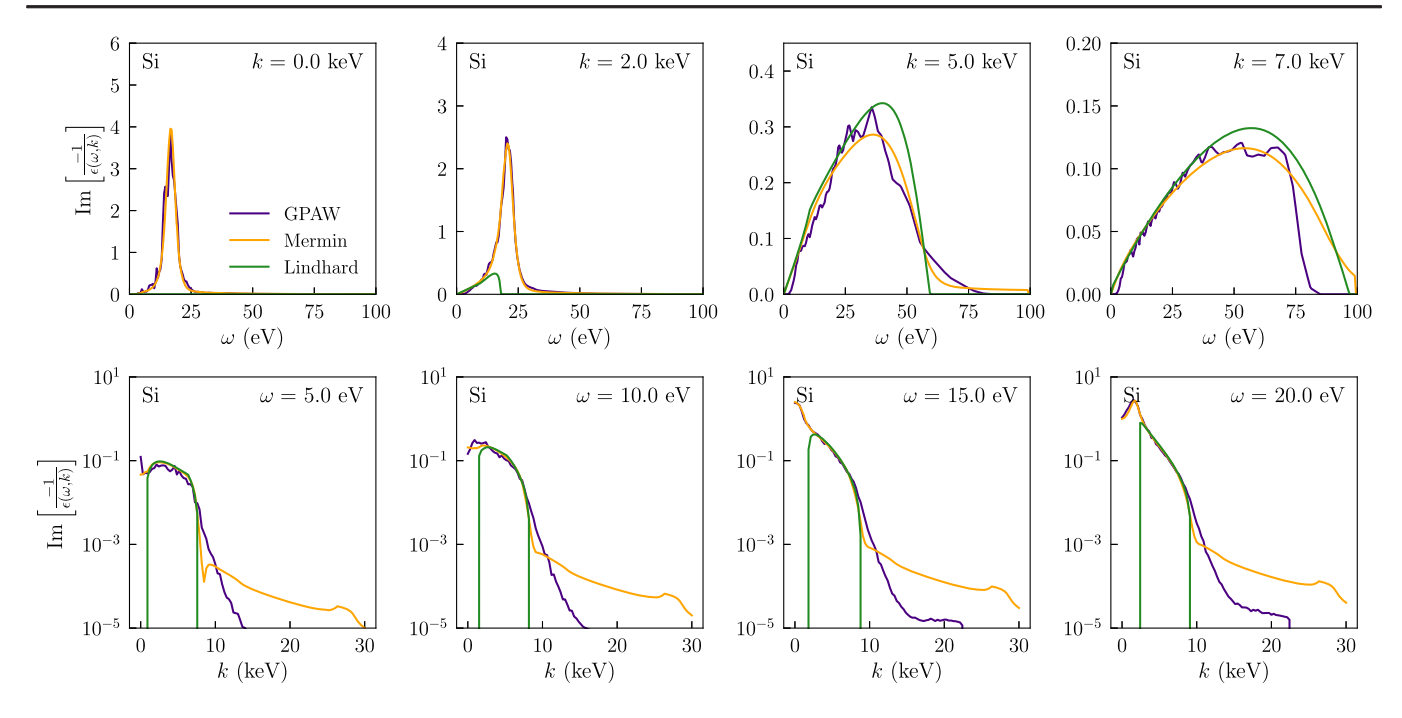


FIG. 2. ELF for Si, calculated using the Lindhard, Mermin and GPAW methods for select values of ω and k.

This is shown in the right-hand panel of Fig. 1, where the band gap is now clearly visible at low ω . The GPAW method is however by far the most computationally intensive of the three and is most the difficult to validate for nonexperts in TDDFT methods. At this time we therefore only provide ELF look-up tables calculated with the GPAW method for Si and Ge.² For more details on our calculations of the ELF in GPAW, we refer the reader to [17].

The limitations and regime of applicability of each method can be made more manifest by taking slices for fixed k and ω , as shown in Fig. 2. In the low k regime (upper left panels) the plasmon peak is clearly visible and we find excellent agreement between the Mermin and GPAW methods. The Lindhard method on the other hand fails spectacularly due to its omission of dissipation effects. For higher values of k (upper right panels) we are firmly in the electron-hole pair regime and all three methods are in fairly good agreement for $\omega \lesssim 25$ eV. The Lindhard method remains in qualitative agreement with the others for higher ω as well, though the approximation is clearly less suitable. Our calculations with the GPAW method are not applicable beyond $\omega \gtrsim 75$ eV since only the 70 lowest laying bands were included for computational reasons.

In the left-hand panel of Fig. 1 and the bottom row of Fig. 2 we see the well-known fact that the Lindhard model does not allow for excitations of electron-hole pairs to be created outside a band in momentum space, whose width is set by the Fermi momentum. We will refer to this band as the Lindhard electron-hole continuum. In the bottom row of Fig. 2 we see that all three methods are in good agreement within this region. In the Mermin and GPAW methods, excitations outside the Lindhard electron-hole continuum are allowed. At lower k values, the Mermin and GPAW methods are also in reasonably good agreement with each other provided that $\omega \gtrsim 5$ eV, well above the electron band gap. For k-values above the Lindhard electron-hole continuum $(k \gtrsim 10 \text{ keV})$ the Mermin and GPAW methods start diverging rather strongly. Both methods are challenged here: For the GPAW method one needs an increasingly large grid in momentum space, which significantly impacts the computational requirements of the calculation. In our calculations we restricted the grid to $k \lesssim 22$ keV, which corresponds to the sharp edge in the two bottom right panels of Fig. 2. Beyond this value we currently do not make a prediction for the ELF, and DarkELF will automatically restrict the phase space of all processes to k values satisfying this constraint.

The Mermin method reproduces the measured Compton spectrum for high momenta ($k \gtrsim 20 \text{ keV}$) and high energy ($\omega \gtrsim 1 \text{ keV}$) [63], though its validity for high k and low ω regime that is of interest for dark matter scattering is less established. In particular, the lower row of Fig. 2 shows that the Mermin method predicts a substantially larger ELF in the high k regime than the GPAW method. As we will see in the next section, this regime is relevant for dark matter experiments with energy thresholds exceeding roughly

²At this time, *DarkELF* only accounts for the diagonal part of the ELF, which more generally is a matrix in reciprocal lattice space. Throughout this paper, \mathbf{k} therefore indicates an arbitrary momentum vector which can be outside the first Brillouin zone, such that $\mathbf{k} \equiv \mathbf{k}' + \mathbf{K}$ with \mathbf{k}' restricted to the first BZ and \mathbf{K} a reciprocal lattice vector. See Ref. [17] for details.

15 eV. This behavior as predicted by the Mermin method is likely not accurate and can be traced back to the rather rigid functional form in (3), as both the k regime above and below the Lindhard electron-hole continuum are controlled by the same set of dissipation parameters. Moreover, the various fits only take into account optical and/or REELS data, which are both probing the low momentum regime.³

Inelastic x-ray scattering measurements on the other hand are a good alternative in the high k regime. Weissker et al. [65] carried out a series of such ELF measurements for Si at European Synchrotron Radiation Facility (ESRF) with an 8 keV x-ray beam. Unfortunately, the momentum transfer they had access to is insufficiently high to diagnose the discrepancy in Fig. 2. In the regime which they do have access to, our calculations are in good agreement with their measurements, see Ref. [17]. They moreover carefully compare their results with a suite of TDDFT calculations and find overall good agreement as well. For these reasons, we assign more credence to our GPAW result in the high k regime, but independent experimental verification with data from a high energy synchotron facility would nevertheless be interesting. In the next sections we will comment in some detail on how these various uncertainties propagate to the dark matter scattering rate.

III. DARK MATTER-ELECTRON SCATTERING

In the section, we briefly summarize the formalism for dark matter-electron scattering as laid out in [17]. We illustrate the functionality and limitations of calculations with *DarkELF* by comparing results obtained with the Lindhard, Mermin, and GPAW methods, as well as a number of different materials. We do not, however, attempt an exhaustive comparison between possible target materials in this paper.

To start, we assume that in the nonrelativistic limit, DM of mass m_{χ} interacts dominantly with the electron number density n by means of a mediator particle ϕ . The interaction Hamiltonian is then

$$H = g_{\nu}\phi\bar{\chi}\chi + g_{\rho}\phi n \tag{4}$$

with n the electron number density operator. The mediator ϕ could represent a scalar mediator or the time-like component of a vector mediator such as a dark photon. This approach makes it explicit that the in-medium response in the nonrelativistic limit is the same for vector and scalar mediators [66]. For this class of models, the dark matter scattering can be written in terms of the dynamic structure factor $S(\omega, \mathbf{k})$, which is defined as

$$S(\omega, \mathbf{k}) = \frac{2\pi}{V} \sum_{i,f} P_i |\langle f | n_{-\mathbf{k}} | i \rangle|^2 \delta(\omega + E_i - E_f), \quad (5)$$

with $n_{-\mathbf{k}}$ the Fourier transform of the electron number density operator and $P_i \equiv e^{-\beta E_i}/Z$ is the thermal occupation number. Here β is the inverse temperature ($\beta \equiv 1/T$), Z the partition function of the system and V its volume. The initial and final states of the system are denoted by $|i\rangle$ and $\langle f|$ respectively, with corresponding energies E_i and E_f . By making use of the fluctuation-dissipation theorem, one can show that the dynamical structure function is related to the ELF by [67]

$$S(\omega, \mathbf{k}) = \frac{k^2}{2\pi\alpha} \frac{1}{1 - e^{-\beta\omega}} \operatorname{Im} \left[\frac{-1}{\epsilon(\omega, \mathbf{k})} \right]. \tag{6}$$

Also folding in the DM velocity distribution, DM scattering form factor and the various flux factors, we arrive at our final expression for the DM scattering rate, in units of number of counts per unit of exposure

$$R = \frac{1}{\rho_T} \frac{\rho_\chi}{m_\chi} \frac{\bar{\sigma}_e}{\mu_{\chi e}^2} \frac{\pi}{\alpha} \int d^3 v f_\chi(v) \int \frac{d^3 \mathbf{k}}{(2\pi)^3} k^2 |F_{\rm DM}(k)|^2$$

$$\times \int \frac{d\omega}{2\pi} \frac{1}{1 - e^{-\beta\omega}} \text{Im} \left[\frac{-1}{\epsilon(\omega, \mathbf{k})} \right] \delta\left(\omega + \frac{k^2}{2m_\chi} - \mathbf{k} \cdot \mathbf{v}\right),$$
(7)

where $f_{\chi}(v)$ is the dark matter velocity distribution, which is taken to correspond to the Standard Halo Model with $v_{\rm esc}=500$ km/s, velocity dispersion $v_0=220$ km/s, and Earth velocity $v_e=240$ km/s. ρ_{χ} is the local DM density, taken to be 0.4 GeV/cm³. The DM-mediator form factor is defined as

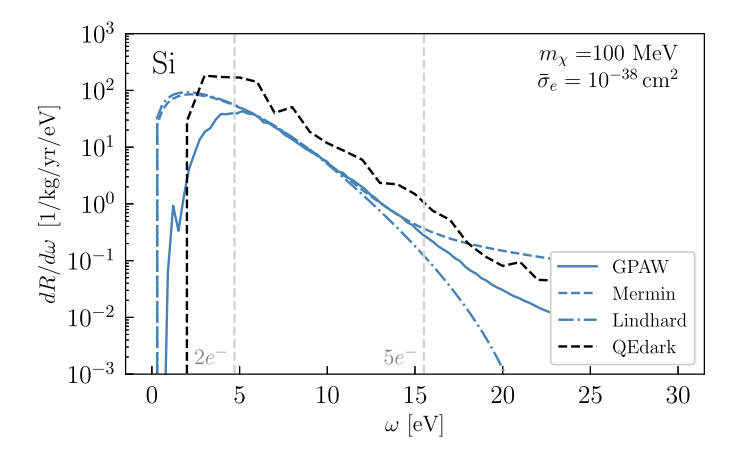
$$F_{\rm DM}(k) = \frac{\alpha^2 m_e^2 + m_\phi^2}{k^2 + m_\phi^2}.$$
 (8)

The limiting cases of $F_{\rm DM}(k)=1$ and $F_{\rm DM}(k)=\alpha^2 m_e^2/k^2$ are most frequently studied and are referred to respectively as the "massive mediator" and "massless mediator" regimes. The user moreover has access to the double differential distribution $d^2R/dkd\omega$, such that more general form factors can be implemented easily. The effective cross section is defined as

$$\bar{\sigma}_e = \frac{\mu_{\chi e}^2 g_e^2 g_{\chi}^2}{\pi (\alpha^2 m_e^2 + m_{\phi}^2)^2}.$$
 (9)

In general, the ELF can depend on the direction of the momentum transfer \mathbf{k} , though for many materials the isotropic approximation is very good. The current version of DarkELF therefore assumes the isotropic limit for $S(\omega, \mathbf{k})$ and the ELF. The generalization to the nonisotropic case is left for future work. The functions provided by DarkELF are summarized in the Appendix. In the functions

 $^{^3}$ REELS measurements do give access to finite k, see, e.g., [64], but the rate is still dominated by low to intermediate k. The unfolding of the experimental results with the inverse Monte Carlo method in [64] therefore likely leads to large systematic uncertainties in the high k regime. Finally, their results are not publicly available in a suitable format and are thus currently not included in our analysis.



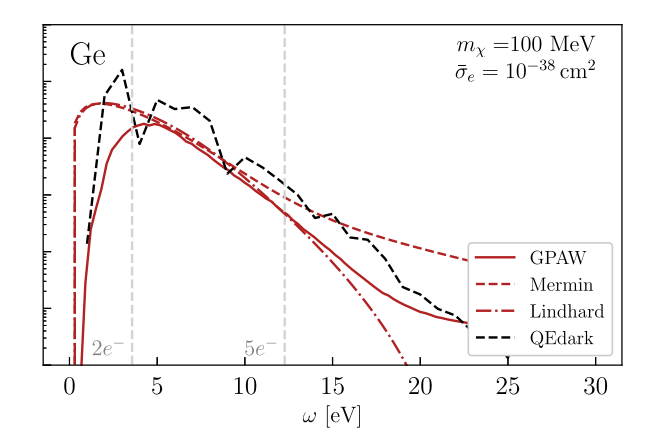


FIG. 3. Comparison between Lindhard, Mermin, and GPAW calculations of the differential scattering rate for Si and Ge, for the massless mediator regime. The vertical dashed lines indicate the $2e^-$ and $5e^-$ thresholds. The black dashed line is obtained with the QEDARK code [10], which does not include screening effects and gives a larger rate.

which compute the (differential) rate, the velocity integral has already been performed, by swapping the order of the integrals in (7).

Figure 3 shows the comparison of the differential scattering rate obtained with the Lindhard, Mermin, and GPAW methods for a benchmark model point. As explained in the previous section, the Lindhard and Mermin methods are less reliable for ω values near the band gap (E_{gap}) , which results in the disagreement for $\omega \lesssim 5$ eV. If we follow the treatment in [10,68] to convert ω into the observed number of ionization electrons, this roughly corresponds to the $2e^-$ threshold. Hence, if the single ionization electron rate is desired, the GPAW method is recommended. That said, even with the GPAW method our current ELF grids are fairly noisy for $\omega \lesssim 2E_{\rm gap}$, and we expect there to be $\mathcal{O}(1)$ theoretical uncertainties. In most experiments, however, large backgrounds are expected in the single electron bin, and the bulk of the sensitivity will come from events with at least two ionization electrons [1,3,18]. With a $2e^-$ threshold and a massless mediator, we find that the Mermin and Lindhard calculations are in good agreement with the GPAW computations.

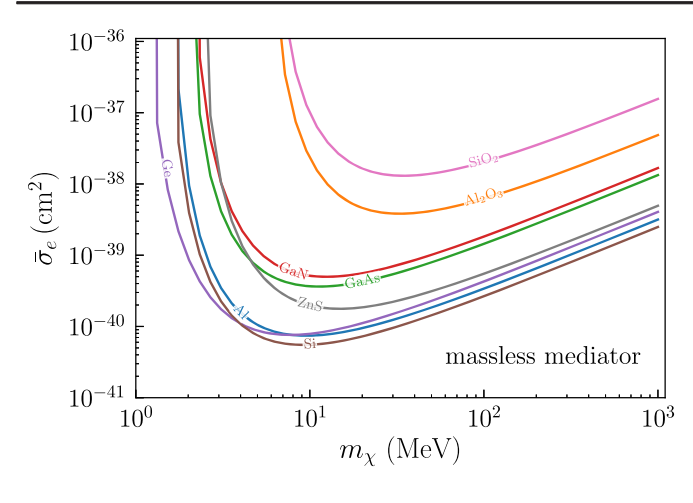
The various methods start diverging for $\omega \gtrsim 15 \, \mathrm{eV}$, which roughly corresponds to 5 ionization electrons in Si. This behavior is caused by the discrepancy at high momenta in the bottom row of Fig. 2. We recommend the GPAW results in this regime. Note that this part of the spectrum is very subleading and is only relevant for experiments with a relatively high energy threshold, or in a post-discovery scenario where one would want to infer DM properties from the shape of the recoil spectrum. Finally, the dashed black curve on Fig. 3 indicates the prediction using the QEDARK code [10]. The discrepancy is due to screening effects which are neglected in the QEDARK calculation. We refer to [17] for a more detailed discussion of this effect. For a massive mediator, the agreement between the three methods is less satisfactory, since the

rate is weighted more toward the high *k* part of the phase space. We thus recommend to use the ELF obtained with GPAW for the massive mediator. Plots of the differential rate for this scenario can be found on our github repository.

We compare the overall fiducial cross section reach of a number of materials in Fig. 4. We hereby assumed the $2e^-$ threshold for Ge, Si, and GaAs and set the threshold to twice the band gap for all other materials except for Al. In the latter case we assumed 5 eV. At present we do not have GPAW results for materials other than Ge and Si, and we therefore used the Mermin method for all materials. The experimental inputs for Si, Al, Al₂O₃, ZnS, and SiO₂ were taken from the Ding *et al.* database [54]. For Ge we used the Novak *et al.* data [53] and the rates for GaAs and GaN were extracted from the measurements by Tung *et al.* [55].

Commonly used targets such as Ge and Si perform favorably as compared to the other materials considered here. While screening effects are stronger in lower-gap semiconductors such as Ge and Si, this is more than compensated for the lower threshold. The weaker reach for the other semiconductors is due in part to the higher $2e^-$ threshold. For instance, the average energy needed per ionization electron is much higher in GaAs compared to the otherwise similar material Ge [68], such that the $2e^-$ threshold is around 6.1 eV as compared to 3.6 eV for Ge. For the other semiconductors, the bandgaps are also higher than in Si and Ge.

The results in Fig. 4 were all obtained with the Mermin method. As noted above, in the massive mediator limit, the rate is sensitive to the high k regime in Fig. 2, for which the reliability of the Mermin method is doubtful. For this reason, we chose to restrict the phase space by imposing $k \lesssim 12$ keV in the massive mediator plot in Fig. 4. The cross section curves shown should thus be interpreted as conservative upper bounds. To remedy this problem, a dedicated DFT calculation would be desirable for all materials of interest to the experimental community, similar



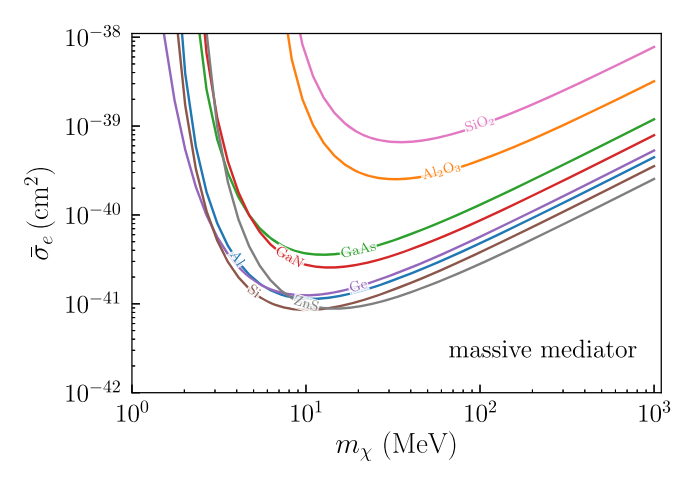


FIG. 4. For DM-electron scattering, a comparison of the cross sections needed to obtain 3 events for a kg-year exposure. For all for 8 materials, the ELF is obtained with the Mermin method. The threshold was taken to be the $2e^-$ threshold for Ge, Si, and GaAs, 5 eV for Al and $2 \times E_{\rm gap}$ for the remaining materials. For the massive mediator, we restricted the phase space to k < 12 keV. As such, these cross sections curves should be viewed as a conservative upper bound.

to the target comparison performed by Griffin *et al.* [15]. The latter results however do not yet include the $\mathcal{O}(1)$ screening effects. We leave such computations for future work.

Details on the usage of *DarkELF* for electron recoil processes can be found in the Appendix.

IV. NUCLEAR RECOILS THROUGH THE MIGDAL EFFECT

The first generations of direct detection experiments were optimized to discover elastic nuclear recoils in a large target volume. For $m_\chi \lesssim 1$ GeV, the energy deposited in the nuclear recoil can however easily be below the detector threshold, and one either has to consider a dedicated, ultralow threshold detector with a low mass target such as liquid He [5,69,70], or make use of inelastic processes such as bremsstrahlung [71] or the Migdal effect [12,25]. The Migdal effect [23,24] refers to the process where the atom shakes off one or more electrons immediately after being struck by an external probe, which in our case is the DM. This process was studied extensively in the context of DM scattering off atomic targets [12–14,25–34] and estimates were obtained for semiconductor targets [28,34].

In atomic targets, the calculation can be performed most conveniently by boosting to the rest frame of the recoiling atom and writing the matrix element in terms of the transition dipole moments for the atom. Ibe *et al.* [26] comprehensively review this formalism in the context of DM scattering and numerically calculated the relevant matrix elements with the Flexible Atomic Code [72]. Whenever we discuss the atomic Migdal effect in this work, we will be referring to the Ibe *et al.* computation, though others are available as well, as referenced above. *DarkELF* incorporates the numerical form factors obtained in [26] and can therefore be used to perform atomic Migdal calculations for select materials.

The Migdal effect in semiconductors is more subtle, due to the delocalized nature of the electron clouds. This prevents one from using the boosting method, as the rest frame of the lattice is now a preferential frame. A full calculation in the rest frame of the lattice was completed simultaneously by us [35] and Liang *et al.* [36] and revealed a qualitatively different answer from directly applying the Ibe *et al.* method to a crystal. In this work we also showed that plasmon production [73,74] is included in the Migdal rate, but is very subleading for a DM candidate with a standard velocity profile.

Here we only present the final result and discuss its regime of validity and implementation in *DarkELF*; for the full derivation and discussion, see Ref. [35]. For a monatomic material, we found that the rate in number of counts per unit exposure is given by

$$R = \frac{8\pi^2 \alpha A^2 \rho_{\chi} \bar{\sigma}_n}{m_N m_{\chi} \mu_{\chi n}^2} \int d^3 v f_{\chi}(v) \int d\omega \int \frac{d^3 \mathbf{q}_N}{(2\pi)^3} \int \frac{d^3 \mathbf{p}_f}{(2\pi)^3} \int \frac{d^3 \mathbf{k}}{(2\pi)^3} \frac{Z_{\text{ion}}(k)^2}{k^2} \text{Im} \left[\frac{-1}{\epsilon(\mathbf{k}, \omega)} \right] \left[\frac{1}{\omega - \frac{\mathbf{q}_N \cdot \mathbf{k}}{m_N}} - \frac{1}{\omega} \right]^2 \times |F_{\text{DM}}(\mathbf{p}_i - \mathbf{p}_f)|^2 |F(\mathbf{p}_i - \mathbf{p}_f - \mathbf{q}_N - \mathbf{k})|^2 \delta(E_i - E_f - E_N - \omega)$$

$$(10)$$

with A, m_N , and $\mu_{\chi n}$ are the mass number of the element, the total mass of the nucleus, and the DM-nucleon reduced mass, respectively. $\bar{\sigma}_n$ is the DM-nucleon reference cross section that is used to parametrize the reach. For example, assuming a scalar mediator with universal couplings to protons and neutrons

$$H = g_{\gamma}\phi\bar{\chi}\chi + g_{n}\phi(n\bar{n} + p\bar{p}), \tag{11}$$

the reference cross section is defined by

$$\bar{\sigma}_n = \frac{\mu_{\chi n}^2 g_n^2 g_\chi^2}{\pi (q_0^2 + m_\phi^2)^2},\tag{12}$$

where m_{ϕ} is the mass of the mediator and q_0 is a reference momentum, which we take to be $q_0 = m_{\gamma} v_0$ with v_0 the DM velocity dispersion. $Z_{ion}(k)$ is the effective charge of the ion, which includes the nucleus and bound core electrons of the atom. In general, the effective charge seen by an external probe depends on its momentum. We extract this momentum dependence from experimental data [75]. The user has the option of switching this momentum dependence off, to facilitate a cleaner comparison with other results in the literature. \mathbf{q}_N , \mathbf{p}_f and \mathbf{k} are the momenta associated with, respectively, the recoiling nucleus, the outgoing DM particle and the electronic excitations. As before, ω is the energy deposited into electronic excitations, while $E_N \equiv q_N^2/2m_N$ is the kinetic energy of the recoiling nucleus. $F_{\rm DM}(\mathbf{p}_i - \mathbf{p}_f)$ is the DM-mediator form factor, which was suppressed in [35]. It is defined as

$$F_{\rm DM}(q) \equiv \frac{q_0^2 + m_\phi^2}{q^2 + m_\phi^2}.$$
 (13)

In a realistic solid, the nucleus is bound to the crystal, which gives rise to the additional crystal form factor $F(\mathbf{p}_i - \mathbf{p}_f - \mathbf{q}_N - \mathbf{k})$ in (10). In [35] we worked in the impulse approximation, which treats the recoiling ion wave function as a plane wave, but accounts for the binding potential through the initial state wave functions [76,77].

This is valid as long as $E_N \gg \bar{\omega}_{\rm ph}$, where $\bar{\omega}_{\rm ph}$ is the average acoustic phonon frequency in the crystal, of order several tens of meV for most materials. In this limit, the crystal form factor can be approximated by

$$F(q) \equiv \left(\frac{4\pi}{\Delta^2}\right)^{3/4} e^{\frac{-q^2}{2\Delta^2}} \tag{14}$$

with $\Delta \equiv \sqrt{m_N \bar{\omega}_{\rm ph}}$. We leave generalizing the calculation beyond the impulse approximation for future work. To avoid extrapolating beyond the regime of validity for the impulse approximation, DarkELF will excise the part of phase space for which E_N is below a threshold value $E_N^{\rm th}$. By default $E_N^{\rm th}$ is taken to be $E_N^{\rm th} = 4\bar{\omega}_{\rm ph}$, as explained in Appendix B of [35], but the user can also test different values by setting the Enth parameter. Finally, we note that the notation in (10) slightly differs from the notation in [35], since here we suppressed the reciprocal lattice vectors, as explained in Sec. II.

The integral in (10) is rather nontrivial to evaluate due to its high dimension and nontrivial boundary conditions. The problem however simplifies substantially if we approximate the target material as isotropic and work in the soft limit where $|\mathbf{q}_N \cdot \mathbf{k}| \ll m_N \omega$ and $k \ll q_N$. Estimating $q_N \sim v m_\chi$, the soft approximation holds for 10 MeV $\lesssim m_\chi \lesssim 10$ GeV and $\omega \gtrsim$ eV, which is the parameter space of interest for the Migdal effect. With these assumptions, (10) can be written as the double differential rate

$$\frac{dR}{dE_N d\omega} \approx \frac{\rho_{\chi}}{m_N m_{\chi}} \int d^3 v v f_{\chi}(v) \frac{d\sigma_{qe}}{dE_N} \frac{dP}{d\omega}, \quad (15)$$

where we defined the quasielastic cross section $\frac{d\sigma_{qe}}{dE_N}$ as

$$\frac{d\sigma_{qe}}{dE_N} = \frac{2\pi^2 A^2 \bar{\sigma}_n}{v \mu_{Nn}^2} \int \frac{d^3 \mathbf{q}_N}{(2\pi)^3} \int \frac{d^3 \mathbf{p}_f}{(2\pi)^3} |F_{\mathrm{DM}}(\mathbf{p}_i - \mathbf{p}_f)|^2 |F(\mathbf{p}_i - \mathbf{p}_f - \mathbf{q}_N)|^2 \delta(E_i - E_f - E_N - \omega) \delta\left(E_N - \frac{q_N^2}{2m_N}\right). \tag{16}$$

For $\omega=0$ this quantity reduces to the elastic nuclear recoil cross section. In limit where the nucleus is taken to be a free particle, or $\bar{\omega}_{\rm ph} \to 0$, the factor $|F(\mathbf{p}_i - \mathbf{p}_f - \mathbf{q}_N)|^2$ moreover asymptotes to $(2\pi)^3 \delta(\mathbf{p}_i - \mathbf{p}_f - \mathbf{q}_N)$; then one recovers the familiar result for the elastic recoil of a free nucleus.

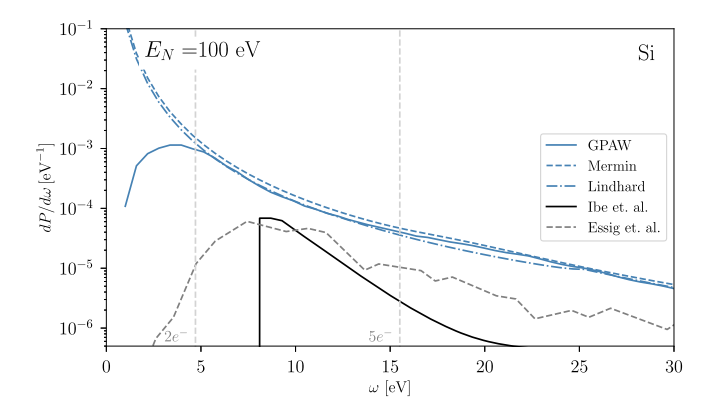
The quantity $dP/d\omega$ is the probability density for energy ω to be deposited into electronic excitations:

$$\frac{dP}{d\omega} = \frac{4\alpha}{\omega^4} \int \frac{d^3 \mathbf{k}}{(2\pi)^3} Z_{\text{ion}}(k)^2 \frac{|\mathbf{v}_N \cdot \mathbf{k}|^2}{k^2} \text{Im} \left(\frac{-1}{\epsilon(\mathbf{k}, \omega)}\right)$$
(17)

$$= \frac{4\alpha E_N}{3\pi^2 \omega^4 m_N} \int dk Z_{\text{ion}}^2(k) k^2 \text{Im} \left(\frac{-1}{\epsilon(k,\omega)}\right)$$
 (18)

where in the second line we have used the isotropic approximation and $v_N^2 = 2E_N/m_N$. The shake-off probability is shown in Fig. 5 for Si and Ge, as computed with the Lindhard, Mermin, and GPAW methods. Above the $2e^-$ threshold all three methods are in good agreement, especially for Si. (The reasons for the discrepancy for $\omega \lesssim 5$ eV were explained in Sec. III.) For comparison, we also show the shake-off probability as obtained using the formalism for the atomic Migdal effect, following [26]. In this calculation one effectively approximates the system as atomic Si/Ge, neglecting the remainder of the lattice. This approach substantially underestimates the shake-off probability in Si and Ge semiconductors, especially at low ω .

To perform the phase space integrals, we define the following auxiliary functions



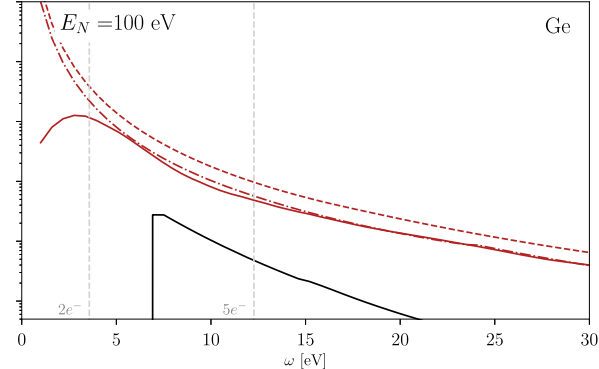


FIG. 5. Shake-off probability for Si and Ge semiconductors as computed with the Lindhard, Mermin, GPAW methods, and for Si and Ge atomic targets using Ibe *et al.* [26]. For comparison, we also show the result in Si semiconductors by Essig *et al.* [28].

$$I(\omega) \equiv \frac{1}{E_N} \frac{dP}{d\omega} \tag{19}$$

$$J(v,\omega) \equiv \int dE_N E_N \frac{d\sigma_{qe}}{dE_N}.$$
 (20)

where $I(\omega)$ is independent of E_N and $J(v,\omega)$ is the energy-weighted quasielastic cross section. Integrating (15) over E_N , the differential rate in ω can be written as

$$\frac{dR}{d\omega} \approx \frac{\rho_{\chi}}{m_{N} m_{\chi}} I(\omega) \int d^{3}v v f_{\chi}(v) J(v, \omega). \tag{21}$$

To speed up the integration, DarkELF will tabulate and interpolate $I(\omega)$ with the default settings whenever a DarkELF object is initialized. If the flag fast is set to True in the Migdal rate calculations, DarkELF will use the precomputed $I(\omega)$ rather than computing it from scratch for each point. The tabulate_I() function can be used to update the precomputed $I(\omega)$ with settings specified by the user. See the Appendix for more details.

It thus remains to evaluate $J(v,\omega)$. In the free ion approximation, the crystal form factor squared asymptotes to a delta function, and we obtain the closed-form expression

$$J(v,\omega) = \frac{A^2 \bar{\sigma}_n}{8 v^2 m_N \mu_{\chi n}^2} (q_0^2 + m_{\phi}^2)^2 \left[\log \left(\frac{q_+^2 + m_{\phi}^2}{q_-^2 + m_{\phi}^2} \right) + \frac{m_{\phi}^2}{q_+^2 + m_{\phi}^2} - \frac{m_{\phi}^2}{q_-^2 + m_{\phi}^2} \right]$$
(22)

with

$$q_{-} = \max \left[v \mu_{\chi N} \left(1 - \sqrt{1 - \frac{2\omega}{v^{2} \mu_{\chi N}}} \right), \sqrt{2m_{N} E_{N}^{\text{th}}} \right]$$

$$q_{+} = v \mu_{\chi N} \left(1 + \sqrt{1 - \frac{2\omega}{v^{2} \mu_{\chi N}}} \right)$$
(23)

with $E_N^{\rm th}$ the energy threshold for the nuclear recoil and $\mu_{\chi N}$ the DM-nucleus reduced mass. Experimentally, $E_N^{\rm th}$ can effectively be zero if one is only interested in the ionization signal. However, theoretically, both the free ion and impulse approximations break down for $E_N^{\rm th} \to 0$ and we therefore use a nonzero $E_N^{\rm th}$, as discussed below (14). In the massive $(m_\phi \to \infty)$ and massless $(m_\phi \to 0)$ limits, $J(v,\omega)$ reduces to

$$J_{\infty}(v,\omega) = \frac{A^2 \bar{\sigma}_n}{16v^2 m_N \mu_{\gamma n}^2} (q_+^4 - q_-^4)$$
 (24)

$$J_0(v,\omega) = \frac{A^2 \bar{\sigma}_n q_0^4}{4v^2 m_N \mu_{\chi_n}^2} \log\left(\frac{q_+}{q_-}\right)$$
 (25)

where the ∞ and 0 subscripts refer to the massive mediator and massless mediator limits, respectively.

The expression for $J(\omega, v)$ in the impulse approximation is more complicated:

$$J(v,\omega) = \frac{A^2 \bar{\sigma}_n}{16\sqrt{\pi} v^2 m_N \mu_{\chi n}^2} \int_{q^-}^{q^+} dq |F_{\rm DM}(q)|^2 \times (G(q, q_N^+) - G(q, q_N^-))$$
 (26)

with

$$G(q, q_N) \equiv 2\Delta (q^2 - qq_N + q_N^2 + \Delta^2) e^{-\frac{(q+q_N)^2}{\Delta^2}}$$

$$-2\Delta (q^2 + qq_N + q_N^2 + \Delta^2) e^{-\frac{(q-q_N)^2}{\Delta^2}}$$

$$+ \sqrt{\pi} q (2q^2 + 3\Delta^2) \text{Erf} \left[\frac{q - q_N}{\Delta}, \frac{q + q_N}{\Delta} \right]$$
 (27)

where the incomplete error function is defined as

$$\operatorname{Erf}(x,y) \equiv \frac{2}{\sqrt{\pi}} \int_{x}^{y} dt e^{-t^{2}}.$$
 (28)

The boundary conditions are given by

$$q_{\pm} = v\mu_{\chi N} \left(1 \pm \sqrt{1 - \frac{2\omega}{v^2 \mu_{\chi N}}} \right)$$

$$q_N^+ = \sqrt{2m_N \left(vq - \frac{q^2}{2m_\chi} - \omega \right)}$$

$$q_N^- = \sqrt{2m_N E_N^{\text{th}}}.$$
(29)

The momentum integral in (26) must be evaluated numerically. As a result, the computation for the impulse approximation is substantially slower than for the free ion approximation.

The cross section plots for a rate of 3 events/kg-year are shown in Fig. 6, where we computed the ELF with the GPAW method and assumed a $2e^-$ threshold. The dashed line is the free ion approximation with $E_N^{\rm th}=4\bar{\omega}_{\rm ph}$. The shaded bands represent the impulse approximation, where we varied $E_N^{\rm th}$ between $4\bar{\omega}_{\rm ph}$ and $9\bar{\omega}_{\rm ph}$ in order to illustrate the sensitivity to the phase space cut on E_N . For $m_\chi \lesssim 30$ MeV this sensitivity becomes very severe and we chose to discontinue the curves. This means that the impulse

approximation is not valid in most of the phase space for $m_\chi \lesssim 30$ MeV, and the wave function of the ion in the crystal must be accounted for in this regime. In other words, the energy scale of the DM-nucleus collision is now of the same order as the typical energy scale of acoustic excitations in the crystal, and the Migdal effect must be described in terms of multiphonon processes. At low m_χ , the soft limit we assumed, $k \ll q_N$, also breaks down, since $dP/d\omega$ has non-negligible contributions from k up to O(10) keV. These sources of uncertainty are much more severe for the massless mediator case, as the DM-mediator form factor biases the rate toward lower momentum transfers and E_N . Similar considerations likely also apply to the Migdal effect in liquid Xe, which may affect the limits in [28,78].

For reference, Fig. 6 also shows the result in the impulse approximation where we boldly took $E_N^{\rm th}=0$ (dotted lines). We emphasize that is an uncontrolled extrapolation, which should *not* be used to obtain sensitivity estimates or limits. It is however useful to understand the robustness of our calculations: In particular, for the massive mediator we see that the dotted line merges with the others for

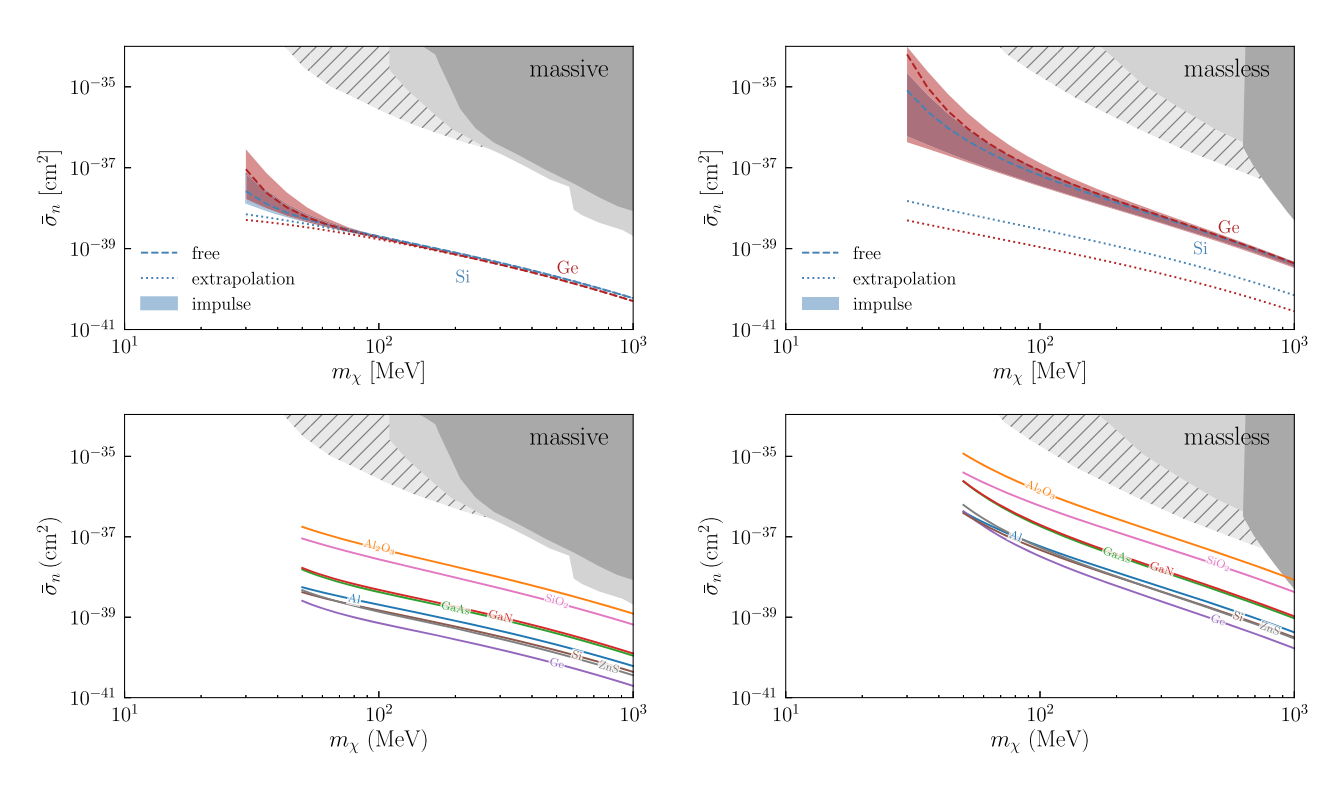


FIG. 6. Upper row: cross section plots for three events with a kg-year exposure, assuming a $2e^-$ threshold, computed with the GPAW method. We show the massive (left) and massless (right) mediator limits. The dashed lines use the free ion approximation with threshold $E_N^{th} = 4\bar{\omega}_{ph}$. The shaded bands use the impulse approximation, varying E_N^{th} between $4\bar{\omega}_{ph}$ and $9\bar{\omega}_{ph}$, which roughly indicates the uncertainty of the approximation. The dotted lines are an (uncontrolled) extrapolation, where we set $E_N^{th} = 0$ in the impulse approximation formulas. (See text for details.) The dark gray shaded regions represent nuclear recoil bounds from XENON1T [78], LUX [79], CRESST III [80], and CDEX [81], while the light gray region is the recent XENON1T limit using the Migdal effect [82]. The hashed regions are recasted XENON limits in terms of the Migdal effect by Essig *et al.* [28]. Bottom row: same as top row, but for a wider range of materials, using the Mermin method and the free ion approximation. For materials with multiple types of atoms, we approximate the rate as coming from the heavier atom.

 $m_{\chi} \gtrsim 70$ MeV. In this regime, the part of phase space removed with the E_N cut is a negligible contribution to the total rate, and we expect the result to be unchanged even if one generalizes the computation beyond the impulse approximation. The same is not true for the massless mediator, where the rate is much more heavily weighted toward lower E_N . In this case, it is necessary to understand the Migdal effect in the multiphonon regime and away from the soft limit to obtain the total rate. Our current calculation can therefore only be used as a conservative estimate for the massless mediator case.

Finally, the lower panels of Fig. 6 show the cross section curves in a wider range of materials, where we assume the free ion approximation with $E_N^{\rm th}=4\bar{\omega}_{\rm ph}$. In materials where there are multiple types of atoms, we estimate the rate by calculating the recoil from the heaviest element only, since we assume that the DM-nucleus cross section scales as A^2 . The lighter element can contribute a comparable amount, so there are O(1) uncertainties in making this approximation. Still, Si and Ge again have the best reach among semiconductors due to the lower $2e^-$ threshold.

V. DARK MATTER-PHONON SCATTERING

For energies below the electron band gap, the ELF of a material is dominated by energy loss into phonon excitations. In this section, we discuss how DM-induced phonon excitations can also be treated with the same approach as introduced in [17] and discussed in Sec. III above. (See also Ref. [18].)

The idea is similar to that of Sec. III, where now we must consider how the mediator couples to protons, neutrons, and electrons. If the mediator couples to these particles in the same proportions as the SM photon, then we can directly extend the formalism of Sec. III and apply (7) below the electron band gap. The intuition behind this result is that an external source can create charge fluctuations in both electrons and ions. The total size of those charge fluctuations determines the dielectric response function $e^{-1}(\mathbf{k},\omega)$ and thus the energy loss rate. For ω above the electron band gap, the response is dominated by electrons since the perturbation to the system happens quickly compared to the characteristic timescale of the ion motion in the crystal, $\sim 1/\bar{\omega}_{\rm ph}$. For energy deposits below the electron band gap, we are in the opposite regime: The response of the electrons is effectively instantaneous on the timescale of the external perturbation. They therefore act as a perfect, dissipationless dielectric. The kinematic degrees of freedom of the ions are now responsible for any energy dissipation in the crystal.

If the mediator couples to the charge fluctuations differently from the SM photon, then the direct relationship to the dielectric response and ELF will be broken. In the most general case, the dynamic structure factor for phonon excitations must be calculated from first principles

according to the mediator couplings. This was discussed in the initial work on this subject [43,44], where it was shown for instance that a kinetically mixed dark photon will lead to optical phonon excitations in polar materials, while a scalar mediator will generally lead to acoustic phonon excitations. The formalism is based closely on the theory of neutron scattering in crystals [83], and further studies of DM-phonon excitations in numerous target materials can be found in Refs. [15,16,49,84].

Therefore, in this work we focus on vector mediators which couple to nucleons and electrons in the same way as SM photon. We will work in the massless mediator limit, motivated by cosmological relic benchmarks such as freeze-in [10,85,86] in this mass range. The data on the ELF in this regime comes from optical measurements at momentum transfer $k \to 0$, and we will approximate the ELF as being independent of k for this calculation. This is a good approximation for sub-MeV dark matter scattering via ultralight mediators, which is strongly weighted at low momentum transfers $k \ll \text{keV}$, and we show below good agreement with the DFT calculations of [44,84]. With these assumptions, (7) simplifies to

$$R = \frac{1}{\rho_T} \frac{\rho_\chi}{m_\chi} \frac{\bar{\sigma}_e}{\mu_{\chi e}^2} \frac{q_0^4}{4\pi\alpha} \int d^3 v \frac{f_\chi(v)}{v} \int \frac{d\omega}{2\pi}$$

$$\times \operatorname{Im} \left[\frac{-1}{\epsilon(\omega)} \right] \log \left[\frac{1 + \sqrt{1 - 2\omega/v^2 m_\chi}}{1 - \sqrt{1 - 2\omega/v^2 m_\chi}} \right] \tag{30}$$

with the reference momentum $q_0 \equiv \alpha m_e$. We also drop the k dependence in the ELF when taking the optical limit.

To make contact with earlier work, we recall that in polar materials, longitudinal optical (LO) phonons generate a long-range polarization in the material, allowing for enhanced interactions with charged particles. For a material such as GaAs with only one LO phonon, the effective coupling of a charged particle with optical phonons is particularly simple and given by the Fröhlich Hamiltonian [87]. The coupling strength of this effective interaction is given by

$$C_F = \sqrt{\frac{\omega_{\text{LO}}}{2} \left(\frac{1}{\epsilon_{\infty}} - \frac{1}{\epsilon_0}\right)}.$$
 (31)

This coupling was discussed in Refs. [43,44] and applied there to DM scattering into single LO phonons. We now show how to obtain the same Fröhlich coupling and DM scattering rate from the ELF, and also generalize it to include multiple optical phonon branches.

To establish the relationship between the ELF and the Fröhlich coupling, we use an analytic approximation for the dielectric function in polar materials. This analytic form is also convenient for materials where suitable low temperature ELF data or first principles calculations are not

readily available. Concretely, we approximate the dielectric function by [88]:

$$\epsilon(\omega) = \epsilon_{\infty} \prod_{\nu} \frac{\omega_{\text{LO},\nu}^2 - \omega^2 - i\omega \gamma_{\text{LO},\nu}}{\omega_{\text{TO},\nu}^2 - \omega^2 - i\omega \gamma_{\text{TO},\nu}},\tag{32}$$

where ν labels an optical phonon branch containing both longitudinal (LO) and transverse (TO) modes. ω_{ν} and γ_{ν} are the energy and width of the phonon mode, respectively. ϵ_{∞} is the high-frequency dielectric constant which describe the contribution of electrons to dielectric response below the band gap; that is, this is the dielectric constant at frequencies well above the phonon energies but still below the electron band gap. Using (32) allows for excellent fits to optical data along high-symmetry directions of polar crystals, but note that for arbitrary wave vectors the notion of purely transverse and longitudinal optical modes may not be well defined. In this work, we will mainly work in the isotropic approximation. In general, first-principles approaches to phonon spectra are needed to calculate the full direction-dependent response function, similar to what was done in Refs. [44,49,84].

As can be seen from the form of (32), the ELF will be dominated by LO phonon resonances. Example ELFs for the polar materials GaAs and SiO_2 (quartz) are shown in Fig. 7. SiO_2 is a birefringent material where the dielectric response depends on the polarization of the incident field with respect to the optical axis (or c-axis), with ordinary rays corresponding to $\vec{E} \perp c$ -axis and extraordinary rays corresponding to $\vec{E} \parallel c$ -axis. For transverse photon modes, this therefore corresponds to optical phonon modes with

 $\mathbf{k} \parallel c$ -axis (ordinary response) or $\mathbf{k} \perp c$ -axis (extraordinary response). To determine the response to DM scattering, we must average over the response in different directions for materials which have anisotropic response, which in principle requires determining the full direction-dependent ELF. However, we find in practice that the rate predictions are very similar whether the ordinary or extraordinary response is used. The same conclusion applies to Al_2O_3 and GaN, which are also birefringent. This is because the rate is usually dominated by a few strong optical phonon modes that do not vary significantly along different directions. For instance, we see that the four strongest modes in the ELF for SiO_2 in Fig. 7 are only shifted slightly between the ordinary and extraordinary response.

To see the connection between the approach here and previous calculations of phonon excitations, note that we can take the narrow phonon width limit since $\gamma_{\nu} \ll \omega_{\nu}$ for all materials here. In this limit, we obtain the loss function

$$\lim_{\gamma \to 0} \operatorname{Im} \left[\frac{-1}{\epsilon(\omega)} \right] = \sum_{\nu} \pi \delta(\omega - \omega_{\text{LO},\nu}) \frac{\omega_{\text{LO},\nu}^2 - \omega_{\text{TO},\nu}^2}{2\epsilon_{\infty} \omega_{\text{LO},\nu}} \times \prod_{\mu \neq \nu} \frac{\omega_{\text{LO},\nu}^2 - \omega_{\text{TO},\mu}^2}{\omega_{\text{LO},\nu}^2 - \omega_{\text{LO},\mu}^2}.$$
(33)

For materials with just a single optical phonon branch, such as GaAs, this simplifies to

$$\lim_{\gamma \to 0} \operatorname{Im} \left[\frac{-1}{\epsilon(\omega)} \right] = \pi \delta(\omega - \omega_{LO}) \times \frac{\omega_{LO}}{2} \left(\frac{1}{\epsilon_{\infty}} - \frac{1}{\epsilon_{0}} \right)$$
$$= \pi \delta(\omega - \omega_{LO}) \times C_{F}^{2}, \tag{34}$$

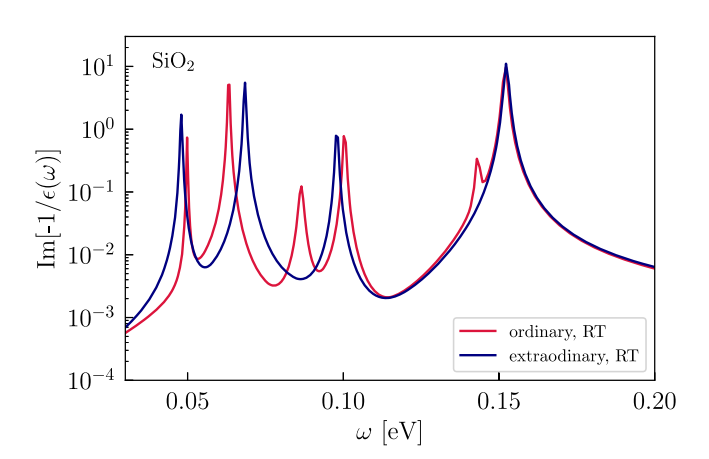


FIG. 7. Examples of the ELF in the phonon regime and in the optical limit $(k \to 0)$. For polar materials, the ELF is dominated by longitudinal optical phonon resonances. Left: the solid line shows the response obtained from the calculation of absorption at 10 Kelvin [89], combined with the real index of refraction [90]. The calculation includes both the optical phonon resonance as well as anharmonic contributions away from the peak. The dashed line shows the response obtained using the analytic approximation of (32), which only partly captures the multiphonon response away from the resonance. Right: we show the response in SiO₂ using (32) with measured parameters of Ref. [91]. The response is shown for ordinary rays $(\vec{E} \perp c$ -axis) and extraordinary rays $(\vec{E} \parallel c$ -axis) at room temperature. The widths of the resonances depend on temperature and will be smaller at zero temperature; however, since the width drops out in the narrow width limit, this has a negligible impact on the DM-phonon scattering rate.

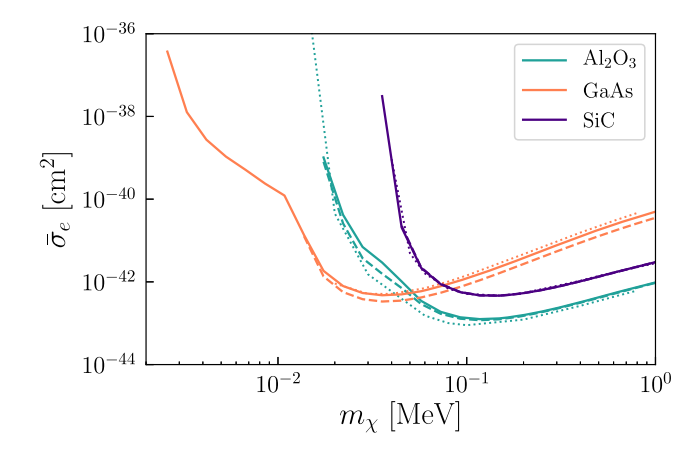


FIG. 8. Comparison of reach in polar materials, taking different approaches to calculating phonon excitations. The lines shown are the 95% CL cross section reach with kg-yr exposure and zero background. The result of numerically integrating the ELF over energy (solid lines) agrees well with the narrow width approximation of (33) (dashed lines). These further agree well with first-principles numerical calculations of phonon scattering (dotted lines), from Refs. [44,84]. In the GaAs, the multiphonon response included in the ELF extends the reach to lower masses.

where in the second line we have identified the Fröhlich coupling C_F discussed above. We have also introduced the static dielectric constant $\epsilon_0 = \epsilon(0) = \epsilon_\infty \omega_{\text{LO}}^2/\omega_{\text{TO}}^2$. While C_F as defined here strictly applies only for simple materials with a single optical phonon branch, we can use (33) more generally given data on the optical phonon frequencies.

Figure 8 compares different approaches to calculating the cross section reach in polar materials. We find good agreement whether we use the full ELF or take the narrow width approximation. (For simplicity, for Al₂O₃ we use the ordinary dielectric response.) Furthermore, our results line up very well with first-principles numerical calculations of phonon scattering, here taken from Ref. [44] for GaAs and Al₂O₃ and from Ref. [84] for SiC. Note that in the case of GaAs, all approaches agree well for masses above ~10 keV. However, the reach determined by numerically integrating the ELF extends to lower masses, because in this case we use a calculation of the ELF that includes the anharmonic multiphonon response below the optical phonon resonance, as shown in Fig. 7. In general, determining the multiphonon response is more challenging, and we only include such contributions where it has been calculated or measured at low temperatures appropriate for a direct detection experiment.

For nonpolar crystals, such as Si and Ge, the optical phonon does not have a long-range polarization and the ELF is instead determined entirely by multiphonon excitations. The ELF determined by theory and experiment is shown in Fig. 9. Note the overall loss rate is several orders of magnitude smaller than for a polar material.

Figure 10 summarizes the phonon excitation reach for all materials considered here, and Table I gives the source of

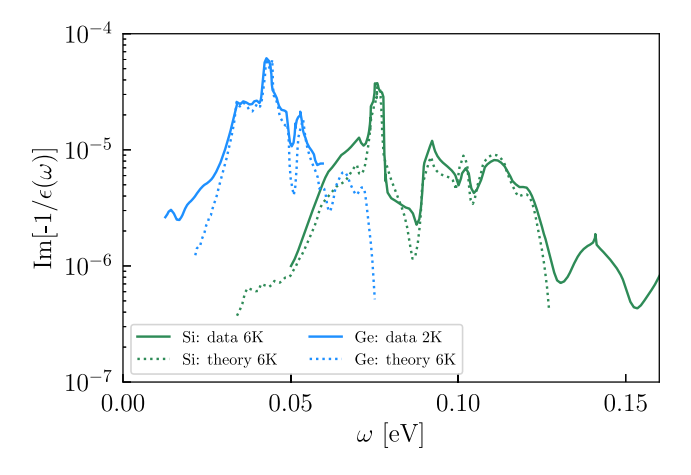


FIG. 9. For nonpolar materials, the optical phonons do not have a long-range polarization and the ELF is instead dominated by multiphonon excitations below the electron band gap. We show the result of optical measurements at 6 K for Si [92] and at 2 K for Ge [93]. The dotted lines show the result of DFT calculations done assuming a temperature of 6 K [94].

the ELF used. Materials like ZnS, SiO₂, and Al₂O₃ have particularly good reach, due to the fact that they contain strong optical phonon modes down to low energies and because they have a relatively low ϵ_{∞} . In particular, $\epsilon_{\infty} = 5.13$ in ZnS, $\epsilon_{\infty} = 2.4$ in SiO₂, and $\epsilon_{\infty} = 3.2$ in Al₂O₃; this correlates with the higher electron band gap in those materials, thus illustrating the mild tension in optimizing the electron recoil signal vs the optical phonon signal in a material.

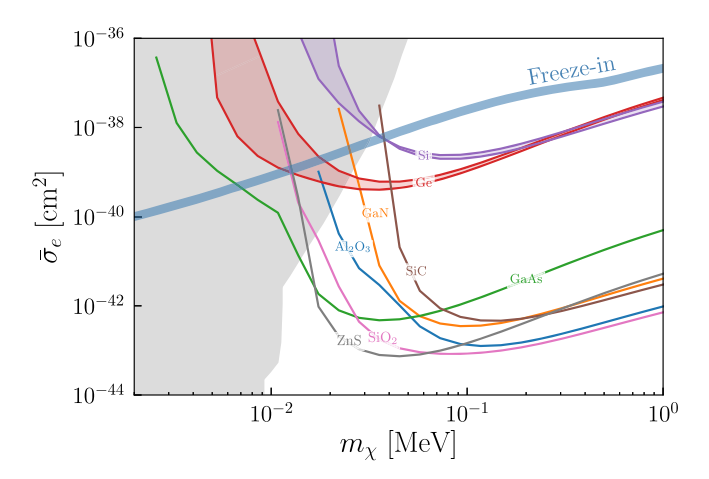
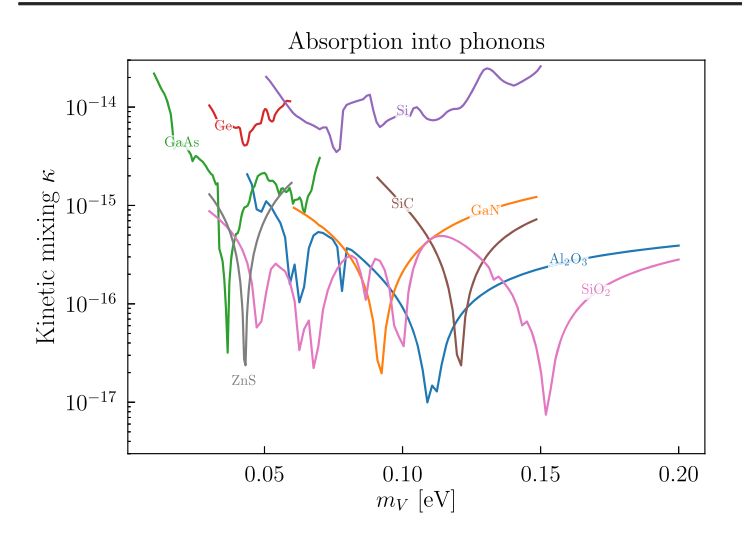


FIG. 10. Comparison of phonon-based reach from DM scattering in all materials considered here. The lines shown are the 95% CL cross section reach with kg-yr exposure and zero background. For Si and Ge, we show both the results obtained using a DFT calculation and using a measurement of the ELF; the region in between is shaded to indicate a rough uncertainty on the true reach. The thick blue line is the predicted cross section if all of the DM was produced by freeze-in [7,85,86]. The grey shaded region corresponds to stellar cooling bounds on this DM candidate [95].



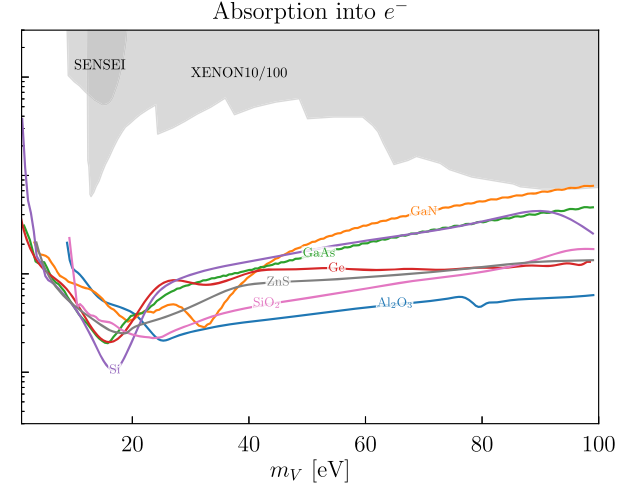


FIG. 11. A comparison of the reach for absorption of kinetically mixed dark photon dark matter. The lines shown are the 95% CL cross section reach with kg-yr exposure and zero background. Left: for phonon excitations, we show here the reach obtained using data on the ELF. As noted in the text, a number of these curves are approximate, given that there is limited data available at zero temperature. Right: we show here the reach for electron excitations using the Mermin oscillator method for the ELF, and there can be small differences in comparing with DFT methods or direct optical measurements. The grey shaded regions are limits from XENON10/100 [104] and SENSEI [1].

Compared to previous studies of the reach in various target materials, the main advantage here is the inclusion of multiphonon excitations, which are challenging and expensive to compute using first-principles phonon codes. Here we make use of previous studies of multiphonon absorption to determine the multiphonon scattering rate in Si, Ge, and GaAs at low masses. Importantly, the approach described here can give a fast and accurate way to estimate the phonon excitation reach given data or theory on the dielectric response in the phonon regime.

VI. ABSORPTION OF BOSONIC DARK MATTER

Dark matter could also be made up of sub-keV bosons, in which case it can be absorbed by the material into phonon or electron excitations. For the specific case where dark matter is comprised of kinetically mixed dark photons⁴ of mass m_V , the absorption rate per unit target mass is also determined by the ELF in the zero-momentum limit and given by [44,100-103]

$$R = \frac{1}{\rho_T} \frac{\rho_{\rm DM}}{m_V} \kappa^2 m_V \text{Im} \left[\frac{-1}{\epsilon(m_V)} \right]$$
 (35)

where κ is the kinetic mixing parameter between the dark and Standard Model photon. Since optical measurements directly probe the zero momentum limit of the dielectric function, previous works used this data to obtain the absorption rate.

DarkELF comes with tabulated ELFs in the optical regime and can therefore be used to quickly obtain the absorption rate. Figure 11 shows the reach obtained for both phonon and electron excitations for materials included in this work. For electron excitations, the data-driven Mermin method includes optical measurements among the data that is being fitted, and we can take the $k \to 0$ limit of the resulting ELF. Because the Mermin dielectric function does not include an electron band gap, we only use the Mermin ELF for $\omega > E_{\rm gap}$.

For phonon excitations, we use the same ELF as discussed in Sec. V and summarized in Table I. Note that some of the data was taken at room temperature and the width of the resonances at sub-Kelvin temperatures will be even smaller. Another caveat to note is that for the

TABLE I. Sources of the ELF in the phonon regime, for different materials. Analytic model refers to (32), where the references cited have fitted optical data in order to determine the parameters in (32) or calculated some of those parameters. Other cases correspond either to direct measurement or DFT-based calculations of dielectric response.

Material	ELF in phonon regime	
Si	6 K data from [92] 6 K calculation from [94]	
Ge	2 K data from [93] 6 K calculation from [94]	
GaAs	10 K calculation of [89], combined with [90]	
Al_2O_3	Analytic model, using data from [88,96]	
$\alpha - SiO_2$	Analytic model, using 300 K data from [91]	
GaN	Analytic model, using 300 K data from [97]	
ZnS	Analytic model, using 300 K data from [98]	
SiC	Analytic model of [84], with data from [99]	

⁴The dielectric function is however also relevant for more general absorption processes such as for scalar mediators, as it parametrizes a reduction in rate due to the screening effects [66].

birefringent materials (Al₂O₃, GaN, and SiO₂) we have taken an average over extraordinary and ordinary response, similar to what was done in Ref. [44]. This is only approximate and properly accounting for the anisotropy of the material would require a first-principles calculation of the ELF, as discussed in Sec. V. However, the strongest resonances in the ELF have only a mild direction dependence (see Fig. 7), so we expect that the averaging done here gives a good approximation.

VII. CONCLUSIONS

We presented *DarkELF*, a PYTHON package to calculate rates for a broad range of DM scattering and absorption processes of interest for direct detection in solid state targets. The unifying feature of these processes is that they are determined by the energy loss function (ELF) of the target material, which characterizes energy loss of Standard Model particles. *DarkELF* computes energy loss rates of dark matter particles using tabulated ELFs. At this time, we include ELF data tables for Al₂O₃, GaN, Al, ZnS, GaAs, SiO₂, Si, and Ge assembled from a combination of data, phenomenological models fitted to data, and first-principles calculations. We aim to add more ELF tables in the future, and our package makes it convenient for users to import their own extractions of the ELF as well.

The currently available dark matter processes, the regime of validity of the calculations, and possible future directions are summarized below:

- (i) DM-electron scattering is determined by the ELF above the electron band gap. We provide ELFs computed in the isotropic limit with a DFT-based method (GPAW) and a data-driven approach (Mermin). Both these approaches start to have large uncertainties at high momentum transfer $(k \gtrsim 20 \text{ keV})$ which impacts DM-electron scattering at high energies ($\omega \gtrsim 15$ eV) and for scattering via massive mediators. In this regime, improved theoretical calculations and/or data extractions are needed. For instance, to increase the reliability of the Mermin method, a dedicated fit to high k data from a high energy synchrotron facility would be desirable. It is also possible to generalize beyond the isotropic approximation and obtain directionally dependent scattering rates, which would give rise to a daily modulation in strongly anisotropic materials.
- (ii) *DM-nucleus scattering with Migdal electrons* depends on the ELF through the probability for a recoiling ion to produce Migdal electrons. The rate to produce Migdal electrons is calculated here for the mass range 30 MeV $\lesssim m_\chi \lesssim$ GeV. This restriction in mass is due in part to the impulse approximation, which treats the recoiling ion wave function as a plane wave. For low nuclear recoil energies that are comparable to typical acoustic phonon energies,

- a calculation of the Migdal effect with multiphonon production is needed. This will be important if we wish to obtain accurate rates for DM-nucleus scattering via massless mediators and for DM masses below 30 MeV.
- (iii) *DM-phonon scattering* is determined by the ELF in the phonon regime, below the electron band gap. Our calculations are valid for DM coupled to a massless kinetically mixed dark photon mediator, since we use ELF data in the optical limit. While there are already many studies with DFT-based calculations of this process, using existing measurements or calculations of the ELF gives a fast and accurate alternate approach. This approach also incorporates multiphonon contributions, which dominate for nonpolar materials and are more challenging to calculate.
- (iv) Absorption of dark photon DM has a rate proportional to the ELF in the optical limit (k=0). Except for the DFT-based calculations in a few cases, the ELFs included are generally obtained either by fitting to optical data or directly from optical data itself. As a result, the ELFs included should describe absorption well in both the phonon and electron regimes.

ACKNOWLEDGMENTS

We thank Kim Berghaus, Brian Campbell-Deem, So Chigusa, Juan Collar, Rouven Essig, Yonit Hochberg, Yoni Kahn, Robert Lasenby, Noah Kurinsky, Toby Opferkuch, Diego Redigolo, Tomer Volansky, and Tien-Tien Yu for useful discussions. We thank Maarten Vos for providing us with a β -version of his CHAPIDIF package and for his assistance with its usage and the interpretation of the results. T. L. is supported by the Department of Energy under grant No. DE-SC0019195 and a UC Hellman fellowship. J. K. is supported by the Department of Energy under grants No. DE-SC0019195 and No. DE-SC0009919.

APPENDIX: USING DARKELF

Here we briefly describe how to run a calculation with *DarkELF*; for details and examples we refer to the github page.

- a. Conventions: Natural particle physics units, with $c = \hbar = 1$. All masses, momenta and energies are in units of eV. Cross sections are to be specified in units of cm².
- b. Dependencies: DarkELF requires PYTHON3.6 or higher, equipped with the numpy [105], scipy [106], pyyaml [107], and pandas [108] packages. The tutorial notebooks require a jupyter [109] installation, but this is in general not needed for DarkELF itself.
- c. Setting up calculation: First be sure that DarkELF directory is in your PYTHON path. To set up a calculation, the user must first load the package

TABLE II. List of public functions in DarkELF that relate to electron recoils. Only mandatory arguments are shown; for optional arguments and flags we refer to the text and the documentation in repository. Some functions are only available for select materials, as indicated in the righthand column. Here Q indicates the number of ionization electrons and Q_{χ} the effective milicharge of the DM, in the massless mediator limit.

Electron recoils					
Function	Description	Available for			
dRdomegadk_electron(omega,k)	$d^2R/d\omega dk$: counts/kg-year × eV ²	All except Xe, SiC, and C			
dRdomega electron(omega)	$dR/d\omega$: counts/(kg-year ×eV)	All except Xe, SiC, and C			
dRdQ electron(Q)	dR/dQ : counts/(kg-year), binned in number of ionization e^-	Si, Ge, and GaAs			
R electron()	R: counts/kg-year	All except Xe, SiC, and C			
electron yield(omega)	Converts energy to number of ionization electrons	Si, Ge, and GaAs			
sigmaebar(Qx,mX)	$\bar{\sigma}_e$ in terms of m_χ and Q_χ for massless dark photon mediator	All except Xe, SiC, and C			

from darkelf import darkelf and subsequently create a darkelf object, which represents a specific target material. This is done by calling the constructor, e.g.,

Si=darkelf(mX=1e8,mMed=0.0,target='Si',
filename='Si_mermin.dat',

phonon_filename='Si_epsphonon_data6K
 .dat')

where the filename refers to the precomputed look-up table for the dielectric function in the electronic regime, and phonon filename sets the look-up table for the phonon regime. The former is tabulated as a function of both ω and k, while the latter only in terms of ω , assuming k = 0. For some materials, DarkELF provides multiple look-up tables for the same ELF, but obtained with different methods, e.g., Mermin vs GPAW. The filename and phonon filename flags allow the user to specify the ELF computation of their choice. It is possible to leave phonon filename and filename unspecified, however in this case the various functions relying on the omitted look-up table will be unavailable. For example, users only interested in e^- recoils or the Migdal effect can leave the phonon filename flag unspecified but must specify filename. The dark matter mass and mediator type will also be set at this stage, respectively with the mX and mMed flags. If they are left unspecified, DarkELF will set them to the default values. The user must create a separate darkelf object for each target material under consideration.

The dark matter and mediator masses stored in the darkelf object can be updated by running the update_params method, for example

Si.update_params (mX=1e7, mMed=1e6) sets the DM and mediator masses to 10 and 1 MeV respectively. As an alternative to setting the mediator mass with the mMed flag, the mediator='massless' or mediator='massive' flags can be used to specify the massless and massive mediator limits respectively.

The real and imaginary parts of the dielectric function and the ELF can be accessed by running

```
Si.eps1(om,k,method='grid')
Si.eps2(om,k,method='grid')
Si.elf(om,k,method='grid')
```

with om and k the energy and momentum, both in units of eV. The method flag can take values grid, Lindhard or phonon, with grid being the default. If the method is grid, then $\epsilon_{1,2}$ are obtained from an interpolation of the grid supplied in the filename flag, Si mermin.dat in the example above. (As the filename indicates, this particular grid was computed with the Mermin method.) This grid applies to the electronic ELF and can be a precomputed grid with the Mermin or GPAW method, or a grid supplied by the user. The Lindhard flag invokes the Lindhard model in (2), which only relies on the plasma frequency. The latter is set in the .yaml file associated with the target material. Finally, if the phonon flag is set, DarkELF will use the phonon ELF, which must be set with the phonon filename flag in the object constructor. The phonon ELF is always computed or measured in the optical limit, and the momentum parameter k is therefore ignored for the method=phonon setting.

d. Electron recoils: DarkELF can compute the overall rate and differential distributions for DM-electron recoils, with the functions listed in Table II. The rate functions allow for optional arguments sigmae, withscreening and method. sigmae allows the user to change the reference cross section, which is by default set to $\bar{\sigma}_e = 10^{-38} \, \mathrm{cm}^2$. The boolean flag withscreening enables the user to turn off screening effects, to facilitate comparison with earlier results in the literature. The default value is withscreening=True. Finally, the method flag allows the user to specify the method used for computing the ELF, which must be either grid or Lindhard (see above).

In addition, dRdomega_electron(omega), dRdQ_electron(Q) and R_electron()+ have the optional argument kcut, which specifies the upper bound on the momentum k that is included in the phase space integral. By default, DarkELF will use the kinematical boundary condition or the endpoint of the ELF grid to cut off the k

TABLE III. List of public functions in *DarkELF* that relate to the Migdal effect. Only mandatory arguments are shown; for optional arguments and flags, see text and the documentation in the repository. Some functions are only available for select materials, as indicated in the righthand column. The Ibe option only is available for Si, Ge, C, and Xe. For C and Xe the grid option is unavailable.

Migdal effect				
Function	Description	Available for		
dPdomegadk (omega, k, En)	$d^2P/d\omega dk$: shake-off probability, in units of $1/eV^2$	All except SiC		
dPdomega(omega,En)	$dP/d\omega$: shake-off probability, in units of 1/eV	All except SiC		
tabulate I()	Tabulates shake-off probability for faster computations	All except SiC		
dRdEn nuclear(En)	dR/dE_N for elastic nuclear recoils, in units of counts/(kg-year × eV)	All		
dRdomega migdal(omega)	$dR/d\omega$ for Migdal effect, in units of counts/(kg-year × eV)	All except SiC		
R_migdal()	R for Migdal effect, in units of counts/kg-year	All except SiC		

TABLE IV. List of public functions in *DarkELF* related to DM-phonon scattering. Only mandatory arguments are shown; for optional arguments and flags, see text and the documentation in repository. Some functions are only available for select materials, as indicated in the righthand column.

DM-phonon scattering					
Function	Description	Available for			
dRdomegadk_phonon(omega,k)	Double differential phonon rate $dR/d\omega dk$ in $1/kg/yr/eV^2$	All except Al, C, and Xe			
dRdomega_phonon(omega)	Differential phonon rate $dR/d\omega$ in 1/kg/yr/eV	All except Al, C, and Xe			
R_phonon()	Total phonon rate in 1/kg/yr	All except Al, C, and Xe			
R_phonon_Frohlich()	Total phonon rate in 1/kg/yr with analytic approximation	All except Al, C, and Xe			

integration, whichever is lower. kcut allows the user to overwrite this behavior, which can be useful if one is interested in comparing rates for the low momentum part of phase space only. Finally, R_electron() has the optional flag threshold, which specifies the lower threshold when integrating over ω . By default, this value is the two e^- threshold for Si, Ge, and GaAs and twice the band gap for the remaining materials. DarkELF also has a few small auxiliary functions which converts the energy ω to the number of ionization electrons following [10], and the a method to convert the effective millicharge of the dark matter to the reference cross section $\bar{\sigma}_e$, in the massless mediator limit.

e. Migdal effect: DarkELF can compute the shake-off probability as well as the overall and differential rate for the Migdal effect. The public functions related to the Migdal effect are listed in Table III. The dPdomegadk, dPdomega and tabulate I functions have optional arguments method, kcut, Nshell Zionkdependence. method can take on the values Lindhard, grid and Ibe. The former two method, as well as the kcut flag, work as described above. The Ibe option returns the shake-off probability computed using the atomic wave functions in Ibe et al. [26]. The Nshell flag must be set to an integer and denotes the number of shells included in the atomic calculation. It is ignored if method is set to Lindhard or grid. Zionkdependence is a boolean, which determines whether the momentum dependence of the effective ion charge is accounted for. If set to true (default), $Z_{ion}(k)$ is interpolated from a

look-up table. If set to False, DarkELF assumes $Z_{\rm ion}$ to be the total number electrons of the element minus its valence electrons, independent of k. This flag only applies for the Lindhard and grid methods.

In addition, dRdomega migdal also takes the optional arguments Enth, sigma n, approximation and fast. Enth corresponds to threshold nuclear recoil energy E_N^{th} and sigma_n is the reference DM-nucleon cross section $\bar{\sigma}_n$. The approximation flag can be set to free or impulse, to toggle between the free ion and impulse approximations. The latter is more accurate though, the former is substantially faster. The fast flag is a Boolean which specifies whether or not the pre-tabulated values for the shake-off probability are used. Setting fast=True speeds up the calculation but can be inconvenient if one desires to compare different settings for the shake-off probability for a small number of example points. Finally, R migdal takes the same arguments as dRdomega migdal, in addition to threshold, which sets the energy threshold for the electronic excitations. Note that currently the Migdal calculation in DarkELF only accounts for the heaviest element in multi-atomic materials such as Al₂O₃ and GaAs, assuming that it dominates when the DM-nucleus cross section scales as A^2 . Generalizing this to include all elements in the crystal is left for future developments.

f. DM-phonon scattering: The double differential, differential, and total DM-phonon scattering rate is computed with the functions dRdomegadk_phonon, dRdomega_phonon, and R_phonon respectively (see Table IV). All three routines accept the optional flag sigmae, which

TABLE V. List of public functions in *DarkELF* that relate to absorption processes. Only mandatory arguments are shown; for optional arguments and flags, see text and the documentation in the repository. Some functions are only available for select materials, as indicated in the righthand column.

Absorption				
Function	Description	Available for		
R_absorption()	Rate for dark photon absorption, in units of counts/kg-year	All except C and Xe		

sets the effective electron cross section defined in (9), in units of cm². The R_phonon_Frohlich function is the same as R_phonon but uses the Fröhlich analytic approximation instead of the ELF method. Note that these rates should only be applied for the massless mediator limit since data at large k is not included for the ELF in the phonon regime.

g. Dark photon absorption: DarkELF can compute the absorption rate for dark photon DM into both phonons and electronic excitations. The computation can be accessed through the R_absorptionroutine (see Table. V), which has one optional parameter kappa, which sets the mixing parameter between the dark photon and the SM photon. DarkELF uses the dark matter mass to automatically determine whether the phonon or electron ELF must be used. R_absorptionreturns 0 if m_{χ} is outside the range of the available ELF grids.

h. Adding new materials and/or look-up tables: To add a new ELF look-up table, simply add the file to the data

folder of the relevant material and load the new grid in the constructor of the darkelf object with the filename or phonon filename flag, as described above. For ELF in the electronic regime, the data format of the look-up table should be a 4 column, tab separated text file, where the columns represent ω , k, ϵ_1 and ϵ_2 , with ω and k in units of eV. For ELFs in the phonon regime, the format is instead ω , ϵ_1 and ϵ_2 . To add a new target material, first create a new subfolder in the data folder named after the material of interest. Then add a .yaml file to the new folder in which one should specify the various global properties of the material, such as the plasma frequency, mass density etc. The name of the .yaml file must match the name of the folder. Any precomputed ELF look-up tables also go in this folder. Finally, the material can be loaded by the setting target flag in the darkelf constructor to the name of the folder corresponding to the new material.

- [1] L. Barak *et al.* (SENSEI Collaboration), Phys. Rev. Lett. **125**, 171802 (2020).
- [2] N. Castelló-Mor (DAMIC-M Collaboration), Nucl. Instrum. Methods Phys. Res., Sect. A **958**, 162933 (2020).
- [3] D. W. Amaral *et al.* (SuperCDMS Collaboration), Phys. Rev. D **102**, 091101 (2020).
- [4] A. Bernstein *et al.*, J. Phys. Conf. Ser. **1468**, 012035 (2020).
- [5] S. A. Hertel, A. Biekert, J. Lin, V. Velan, and D. N. McKinsey, Phys. Rev. D 100, 092007 (2019).
- [6] C. W. Fink et al., AIP Adv. 10, 085221 (2020).
- [7] R. Essig, J. Mardon, and T. Volansky, Phys. Rev. D 85, 076007 (2012).
- [8] P. W. Graham, D. E. Kaplan, S. Rajendran, and M. T. Walters, Phys. Dark Universe 1, 32 (2012).
- [9] R. Essig, A. Manalaysay, J. Mardon, P. Sorensen, and T. Volansky, Phys. Rev. Lett. 109, 021301 (2012).
- [10] R. Essig, M. Fernandez-Serra, J. Mardon, A. Soto, T. Volansky, and T.-T. Yu, J. High Energy Phys. 05 (2016) 046
- [11] S. K. Lee, M. Lisanti, S. Mishra-Sharma, and B. R. Safdi, Phys. Rev. D 92, 083517 (2015).
- [12] J. D. Vergados and H. Ejiri, Phys. Lett. B **606**, 313 (2005).

- [13] C. C. Moustakidis, J. D. Vergados, and H. Ejiri, Nucl. Phys. B727, 406 (2005).
- [14] H. Ejiri, C. C. Moustakidis, and J. D. Vergados, Phys. Lett. B 639, 218 (2006).
- [15] S. M. Griffin, K. Inzani, T. Trickle, Z. Zhang, and K. M. Zurek, Phys. Rev. D 101, 055004 (2020).
- [16] T. Trickle, Z. Zhang, K. M. Zurek, K. Inzani, and S. Griffin, J. High Energy Phys. 03 (2020) 036.
- [17] S. Knapen, J. Kozaczuk, and T. Lin, Phys. Rev. D 104, 015031 (2021).
- [18] Y. Hochberg, Y. Kahn, N. Kurinsky, B. V. Lehmann, T. C. Yu, and K. K. Berggren, Phys. Rev. Lett. 127, 151802 (2021).
- [19] J. J. Mortensen, L. B. Hansen, and K. W. Jacobsen, Phys. Rev. B 71, 035109 (2005).
- [20] J. Enkovaara *et al.*, J. Phys. Condens. Matter **22**, 253202 (2010).
- [21] N. D. Mermin, Phys. Rev. B 1, 2362 (1970).
- [22] M. Vos and P. Grande, Chapidif Program (to be published).
- [23] A. Migdal, Sov. Phys. JETP 9, 1163 (1939).
- [24] A. B. Migdal, *Qualitative Methods in Quantum Theory* (CRC Press, Boca Raton, 1977), Vol. 48.
- [25] R. Bernabei et al., Int. J. Mod. Phys. A 22, 3155 (2007).

- [26] M. Ibe, W. Nakano, Y. Shoji, and K. Suzuki, J. High Energy Phys. 03 (2018) 194.
- [27] M. J. Dolan, F. Kahlhoefer, and C. McCabe, Phys. Rev. Lett. **121**, 101801 (2018).
- [28] R. Essig, J. Pradler, M. Sholapurkar, and T.-T. Yu, Phys. Rev. Lett. 124, 021801 (2020).
- [29] N. F. Bell, J. B. Dent, J. L. Newstead, S. Sabharwal, and T. J. Weiler, Phys. Rev. D 101, 015012 (2020).
- [30] Z.-L. Liang, L. Zhang, F. Zheng, and P. Zhang, Phys. Rev. D 102, 043007 (2020).
- [31] D. Baxter, Y. Kahn, and G. Krnjaic, Phys. Rev. D 101, 076014 (2020).
- [32] G. Grilli di Cortona, A. Messina, and S. Piacentini, J. High Energy Phys. 11 (2020) 034.
- [33] K. D. Nakamura, K. Miuchi, S. Kazama, Y. Shoji, M. Ibe, and W. Nakano, Prog. Theor. Exp. Phys. 2021, 013C01 (2021).
- [34] C. P. Liu, C.-P. Wu, H.-C. Chi, and J.-W. Chen, Phys. Rev. D 102, 121303 (2020).
- [35] S. Knapen, J. Kozaczuk, and T. Lin, Phys. Rev. Lett. 127, 081805 (2021).
- [36] Z.-L. Liang, C. Mo, F. Zheng, and P. Zhang, Phys. Rev. D 104, 056009 (2021).
- [37] K. Schutz and K. M. Zurek, Phys. Rev. Lett. 117, 121302 (2016).
- [38] S. Knapen, T. Lin, and K. M. Zurek, Phys. Rev. D 95, 056019 (2017).
- [39] F. Acanfora, A. Esposito, and A. D. Polosa, Eur. Phys. J. C 79, 549 (2019).
- [40] A. Caputo, A. Esposito, and A. D. Polosa, Phys. Rev. D **100**, 116007 (2019).
- [41] A. Caputo, A. Esposito, E. Geoffray, A. D. Polosa, and S. Sun, Phys. Lett. B 802, 135258 (2020).
- [42] A. Caputo, A. Esposito, F. Piccinini, A. D. Polosa, and G. Rossi, Phys. Rev. D 103, 055017 (2021).
- [43] S. Knapen, T. Lin, M. Pyle, and K. M. Zurek, Phys. Lett. B **785**, 386 (2018).
- [44] S. Griffin, S. Knapen, T. Lin, and K. M. Zurek, Phys. Rev. D 98, 115034 (2018).
- [45] B. Campbell-Deem, P. Cox, S. Knapen, T. Lin, and T. Melia, Phys. Rev. D **101**, 036006 (2020); **102**, 019904(E) (2020).
- [46] P. Cox, T. Melia, and S. Rajendran, Phys. Rev. D **100**, 055011 (2019).
- [47] A. Mitridate, T. Trickle, Z. Zhang, and K. M. Zurek, Phys. Rev. D 102, 095005 (2020).
- [48] T. Trickle, Z. Zhang, and K. M. Zurek, arXiv:2009.13534.
- [49] A. Coskuner, T. Trickle, Z. Zhang, and K.M. Zurek, arXiv:2102.09567.
- [50] S. Knapen, T. Lin, and K. M. Zurek, Phys. Rev. D 96, 115021 (2017).
- [51] https://jupyter.org/try.
- [52] M. Dressel and G. Gruner, *Electrodynamics of Solids*, 2nd ed. (Cambridge University Press, Cambridge, England, 2003).
- [53] M. Novák, L. Kövér, S. Egri, I. Cserny, J. Tóth, D. Varga, and W. Drube, J. Electron Spectrosc. Relat. Phenom. 163, 7 (2008).
- [54] Y. Sun, H. Xu, B. Da, S.-F. Mao, and Z.-J. Ding, Chin. J. Chem. Phys. 9, 663 (2016).

- [55] Y. Tu, C. Kwei, and C. Tung, Surf. Sci. 601, 865 (2007).
- [56] M. Vos and P.L. Grande, Surf. Interface Anal. 49, 809 (2017).
- [57] I. Abril, R. Garcia-Molina, C. D. Denton, F. J. Pérez-Pérez, and N. R. Arista, Phys. Rev. A 58, 357 (1998).
- [58] M. Vos and P. L. Grande, J. Phys. Chem. Solids 124, 242 (2019).
- [59] I. Abril, C. D. Denton, P. de Vera, I. Kyriakou, D. Emfietzoglou, and R. Garcia-Molina, Nucl. Instrum. Methods Phys. Res., Sect. B 268, 1763 (2010).
- [60] Z. H. Levine and S. G. Louie, Phys. Rev. B 25, 6310 (1982).
- [61] M. Vos and P. L. Grande, J. Phys. Chem. Solids 104, 192 (2017).
- [62] W. Kohn and L. J. Sham, Phys. Rev. 140, A1133 (1965).
- [63] M. Vos, Nucl. Instrum. Methods Phys. Res., Sect. B 366, 6 (2016).
- [64] L. H. Yang, K. Tőkési, J. Tóth, B. Da, H. M. Li, and Z. J. Ding, Phys. Rev. B 100, 245209 (2019).
- [65] H.-C. Weissker, J. Serrano, S. Huotari, E. Luppi, M. Cazzaniga, F. Bruneval, F. Sottile, G. Monaco, V. Olevano, and L. Reining, Phys. Rev. B 81, 085104 (2010).
- [66] G. B. Gelmini, V. Takhistov, and E. Vitagliano, Phys. Lett. B 809, 135779 (2020).
- [67] P. Nozières and D. Pines, Phys. Rev. 113, 1254 (1959).
- [68] C. A. Klein, J. Appl. Phys. 39, 2029 (1968).
- [69] W. Guo and D. N. McKinsey, Phys. Rev. D 87, 115001 (2013).
- [70] Y.-S. Liu, D. McKeen, and G. A. Miller, Phys. Rev. Lett. 117, 101801 (2016).
- [71] C. Kouvaris and J. Pradler, Phys. Rev. Lett. 118, 031803 (2017).
- [72] M. F. Gu, Can. J. Phys. 86, 675 (2008).
- [73] N. Kurinsky, D. Baxter, Y. Kahn, and G. Krnjaic, Phys. Rev. D 102, 015017 (2020).
- [74] J. Kozaczuk and T. Lin, Phys. Rev. D 101, 123012 (2020).
- [75] P. J. Brown, A. G. Fox, E. N. Maslen, M. A. O'Keefe, and B. T. M. Willis, Intensity of diffracted intensities, in *International Tables for Crystallography* (Wiley, 2006), Chap. 6.1, pp. 554–595.
- [76] J. M. F. Gunn and M. Warner, Z. Phys. B 56, 13 (1984).
- [77] G. I. Watson, J. Phys. Condens. Matter 8, 5955 (1996).
- [78] E. Aprile *et al.* (XENON Collaboration), Phys. Rev. Lett. **123**, 241803 (2019).
- [79] D. Akerib *et al.* (LUX Collaboration), Phys. Rev. Lett. **122**, 131301 (2019).
- [80] A. H. Abdelhameed *et al.* (CRESST Collaboration), Phys. Rev. D **100**, 102002 (2019).
- [81] Z. Z. Liu *et al.* (CDEX Collaboration), Phys. Rev. Lett. 123, 161301 (2019).
- [82] E. Aprile *et al.* (XENON Collaboration), Phys. Rev. Lett. 123, 251801 (2019).
- [83] H. Schober, J. Neutron Res. 17, 109 (2014).
- [84] S. M. Griffin, Y. Hochberg, K. Inzani, N. Kurinsky, T. Lin, and T. Chin, Phys. Rev. D 103, 075002 (2021).
- [85] C. Dvorkin, T. Lin, and K. Schutz, Phys. Rev. D 99, 115009 (2019).
- [86] C. Dvorkin, T. Lin, and K. Schutz, Phys. Rev. Lett. 127, 111301 (2021).
- [87] H. Fröhlich, Adv. Phys. 3, 325 (1954).

- [88] F. Gervais and B. Piriou, J. Phys. C 7, 2374 (1974).
- [89] H. M. Lawler and E. L. Shirley, Phys. Rev. B 70, 245209 (2004).
- [90] E. D. Palik, in *Handbook of Optical Constants of Solids*, edited by E. D. Palik (Elsevier, New York, 1985), pp. 429–443.
- [91] F. Gervais and B. Piriou, Phys. Rev. B 11, 3944 (1975).
- [92] M. Ikezawa and M. Ishigame, J. Phys. Soc. Jpn. 50, 3734 (1981).
- [93] M. Ikezawa and T. Nanba, J. Phys. Soc. Jpn. 45, 148 (1978).
- [94] E. L. Shirley and H. M. Lawler, Phys. Rev. B **76**, 054116 (2007).
- [95] H. Vogel and J. Redondo, J. Cosmol. Astropart. Phys. 02 (2014) 029.
- [96] M. Schubert, T. E. Tiwald, and C. M. Herzinger, Phys. Rev. B 61, 8187 (2000).
- [97] G. Yu, N. L. Rowell, and D. J. Lockwood, J. Vacuum Sci. Technol. A 22, 1110 (2004).
- [98] L. Thamizhmani, A. K. Azad, J. Dai, and W. Zhang, Appl. Phys. Lett. 86, 131111 (2005).
- [99] H. Mutschke, A. C. Andersen, D. Clement, T. Henning, and G. Peiter, Astron. Astrophys. 345, 187 (1999).

- [100] H. An, M. Pospelov, and J. Pradler, Phys. Rev. Lett. 111, 041302 (2013).
- [101] H. An, M. Pospelov, J. Pradler, and A. Ritz, Phys. Lett. B 747, 331 (2015).
- [102] Y. Hochberg, T. Lin, and K. M. Zurek, Phys. Rev. D 94, 015019 (2016).
- [103] Y. Hochberg, T. Lin, and K. M. Zurek, Phys. Rev. D 95, 023013 (2017).
- [104] I. M. Bloch, R. Essig, K. Tobioka, T. Volansky, and T.-T. Yu, J. High Energy Phys. 06 (2017) 087.
- [105] C. R. Harris et al., Nature (London) 585, 357 (2020).
- [106] P. Virtanen et al., Nat. Methods 17, 261 (2020).
- [107] https://pyyaml.org/.
- [108] Wes McKinney, in *Proceedings of the 9th Python in Science Conference, Austin, Texas*, edited by Stéfan van der Walt and Jarrod Millman (2010), pp. 56–61.
- [109] T. Kluyver, B. Ragan-Kelley, F. Pérez, B. Granger, M. Bussonnier, J. Frederic, K. Kelley, J. Hamrick, J. Grout, S. Corlay, P. Ivanov, D. Avila, S. Abdalla, and C. Willing, in *Positioning and Power in Academic Publishing: Players, Agents and Agendas*, edited by F. Loizides and B. Schmidt (IOS Press, 2016), pp. 87–90.